THE $Cu_{47}Ti_{34}Zr_{11}Ni_8$ GLASS-FORMING ALLOY: THERMOPHYSICAL PROPERTIES, CRYSTALLIZATION, AND THE EFFECT OF SMALL ALLOYING ADDITIONS ON THE THERMAL STABILITY

Thesis by

Stephen C. Glade

In Partial Fulfillment of the Requirements

for the Degree of

Doctor of Philosophy

California Institute of Technology

Pasadena, California

2001

(submitted August 17 , 2000)

ACKNOWLEDGEMENTS

I gratefully acknowledge Professor Bill Johnson, my research advisor, for giving me the opportunity to pursue my doctorate at Caltech. His enthusiasm for and insight into science are remarkable.

A large part of the data presented in this thesis was collected on the NASA MSL-1 space shuttle mission (Grant No. NAG8-1182). Team TEMPUS, especially David Lee, Rainer Wunderlich, Bob Hyers, and Gerardo Trapaga, helped make these experiments successful. The field ion microscopy/atom probe tomography work was performed at Oak Ridge National Laboratory under the SHaRE program, with the help of Mike Miller and Kaye Russell. The alloy addition work was supported by the U.S. Department of Energy (Grant No. DEFG0386ER45242-DOE).

Carol Garland, with her expertise on the transmission electron microscope, was invaluable in performing much of this work. Also important in my training on the transmission electron microscope were Brent Fultz, Channing Ahn, and Michele Ostraat.

I thank Peter Bogdanoff, Sven Bossuyt, Jonathan Burrows, Haein Choi-Yim, Dale Conner, Rich Dandliker, Chuck Hays, Adrian Hightower, Jörg Löffler, and Andy Waniuk for their assistance in the laboratory, useful discussions, and fruitful collaborations. Ralf Busch was especially helpful in the thermodynamics work, both in preparing for my candidacy examination and this work. Pam Albertson kept the third floor of Keck running smoothly. I also thank all of the members of the Materials Science Option for making my stay at Caltech more enjoyable.

This work would not have been completed without the support and encouragement of my friends and family.

ABSTRACT

The thermophysical properties, crystallization, and the effect of small alloying additions on the thermal stability of $Cu_{47}Ti_{34}Zr_{11}Ni_8$ were investigated. The thermophysical properties studied were specific heat capacity and viscosity. From the specific heat capacity data, the differences in the thermodynamic functions between the liquid and the crystalline states of $Cu_{47}Ti_{34}Zr_{11}Ni_8$ were calculated. A lower Gibbs free energy difference between the liquid and the crystalline states generally indicates a better glass-forming ability of an alloy. A lower entropy of fusion indicates a better glass-forming ability as well. The viscosity data, using the strong/fragile classification of glasses, also give a measure of the glass-forming ability of the alloy.

The crystallization of amorphous $Cu_{47}Ti_{34}Zr_{11}Ni_8$ was studied with many experimental techniques. Similar to other metallic glass-forming alloys, $Cu_{47}Ti_{34}Zr_{11}Ni_8$ phase separates prior to crystallization. $Cu_{47}Ti_{34}Zr_{11}Ni_8$ decomposes to copper-enriched and titanium-enriched regions (the copper-enriched regions are low in titanium and vice versa). Primary crystallization of $Cu_{47}Ti_{34}Zr_{11}Ni_8$ consists of face centered cubic nanocrystals growing in an amorphous matrix.

The glass-forming ability of certain metallic glass-forming alloys has been improved with small silicon additions, which has been attributed to silicon destabilizing oxide nucleation sites. To investigate this further, a study of the effect of silicon on the crystallization of $Cu_{47}Ti_{34}Zr_{11}Ni_8$ was performed. Prior to crystallization, both $Cu_{47}Ti_{34}Zr_{11}Ni_8$ and $Cu_{47}Ti_{33}Zr_{11}Ni_8Si_1$ phase separate to copper-enriched and titanium-enriched regions. A face centered cubic phase then nucleates and grows in both alloys.

No change in the local composition around a silicon atom in $Cu_{47}Ti_{33}Zr_{11}Ni_8Si_1$ was detected.

Small additions of magnesium and germanium were added to $Cu_{47}Ti_{34}Zr_{11}Ni_8$ to observe the effect on the thermal stability of the alloy. In contrast to the results observed with silicon, no improvement in the glass-forming ability was observed. However, there was an improvement in the thermal stability of the alloy against crystallization in the supercooled liquid regime with both the magnesium and germanium additions.

CONTENTS

FIGURES

TABLES

1. INTRODUCTION

A glass is an amorphous solid. Amorphous solids differ from crystalline solids in that they lack long range atomic order, or translational periodicity. Amorphous solids can be formed using many different processing methods, such as chemical vapor deposition, sputtering, thermal evaporation, and irradiation. The term 'glass' is used for amorphous solids formed by melt quenching.

To form a glass from the liquid state, the liquid must be cooled to the glass transition temperature at a cooling rate fast enough to avoid nucleation and growth of a crystalline phase. Both the thermodynamics and the kinetics of the material influence the process of vitrification. Some materials require relatively low cooling rates to form a glass; SiO_2 requires a cooling rate of 10^{-4} K/s [1]. However, to form an elemental metal into a glass, an estimated cooling rate of 10^{10} K/s is needed [1]. Duwez et al. [2] formed the first metallic glass from the melt, with a composition $Au_{75}Si_{25}$, using an apparatus that cooled the molten metal at a rate of ~10^6 K/s.

This large difference in the cooling rates needed for glass formation in SiO_2 (10^{-4} K/s) versus binary metallic glass-forming alloys (~10^6 K/s) can be understood as follows. In SiO_2, each silicon atom forms bonds with four oxygen atoms, forming a continuous random network [3]. It is relatively difficult for the atoms in this system to arrange themselves in a crystalline phase due to the interconnectedness of the system. Metals, on the other hand, form relatively simple crystal structures, such as body centered cubic (bcc), face centered cubic (fcc), and hexagonal close packed (hcp) phases. Considering

the atoms as hard spheres, it is not difficult for the atoms in a pure metal or a binary alloy to arrange themselves into a crystalline phase.

Recently, multicomponent alloys that require cooling rates as low as 0.1 K/s to form a glass have been developed [4, 5, 6]. These new metallic glass-forming alloys are more stable against crystallization than binary metallic alloys. This can be seen in the time-temperature-transformation (TTT) diagrams, shown in Fig. 1, for a binary alloy and $Zr_{41.2}Ti_{13.8}Cu_{12.5}Ni_{10}Be_{22.5}$, one of these new multicomponent alloys. To form a glass, the liquid must be cooled at a rate fast enough to avoid the nose of the curve, where nucleation and growth of a crystalline phase will occur.

The increased stability of these new metallic glass-forming alloys allows experiments to be performed in the supercooled liquid state that were previously not possible due to crystallization of the metal. Thermophysical properties, including specific heat capacity, viscosity, atomic diffusion coefficients, and the thermal expansion coefficient, have been measured for some of these metallic glass-forming alloys. This allows for the study of glass formation in these alloys as well as the possibility of improving the glass-forming ability of an alloy. Glass-forming ability is defined as the ability of a liquid to avoid crystallization when cooling the melt to the glass transition temperature. Compositions with good glass-forming ability require lower cooling rates than compositions with poor glass-forming ability.

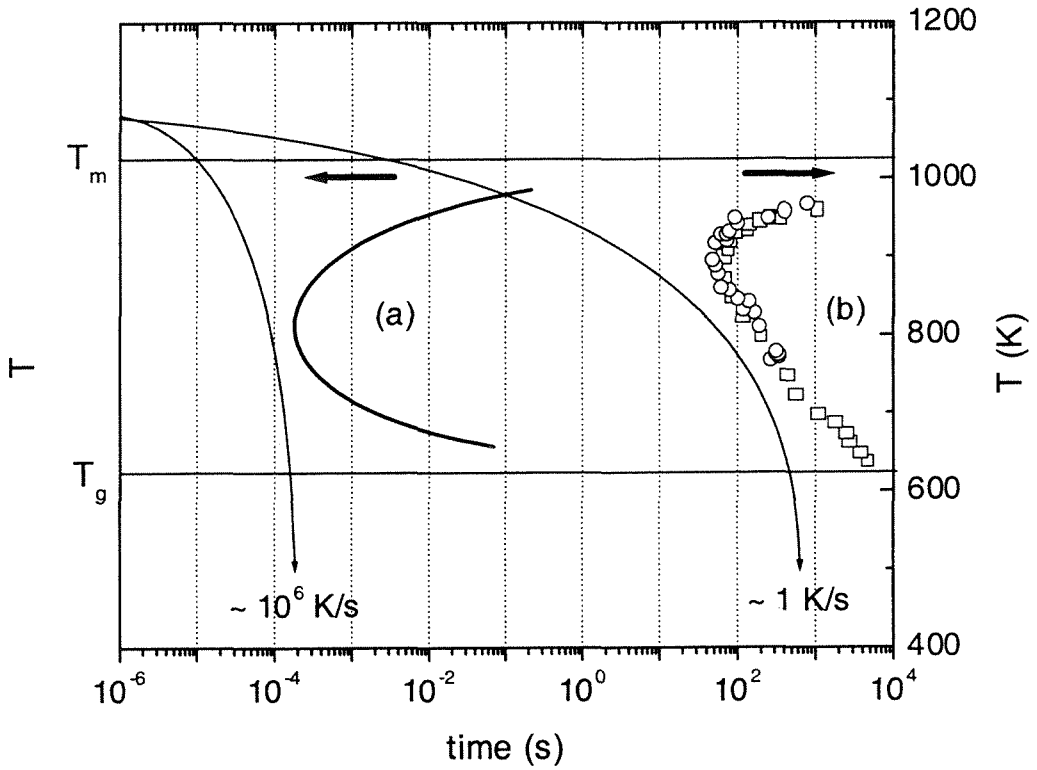

Fig. 1 Schematic time-temperature-transformation (TTT) diagrams for (a) a binary metallic glass-forming alloy and (b) $Zr_{41.2}Ti_{13.8}Cu_{12.5}Ni_{10}Be_{22.5}$

Curve (a) is a hypothetical TTT curve for a binary metallic glass-forming alloy, and curve (b) is data from $Zr_{41.2}Ti_{13.8}Cu_{12.5}Ni_{10}Be_{22.5}$ *[7]. The two cooling curves (curves with the arrows) on the figure show the cooling history needed for glass formation in each system.*

Inoue [8] has proposed three empirical rules for glass formation in metallic systems:

1. The alloys consist of three or more elements.
2. The atomic sizes of the elements differ by at least 12%.
3. The elements have a large negative heat of mixing; i.e., the alloy systems have deep eutectics.

The first two rules are summarized in the 'confusion principle' [9], which states that increasingly complex alloy systems crystallize into increasingly complex crystalline phases. These more complex crystalline phases inhibit crystallization in the system, improving the glass-forming ability of the alloy.

In systems with deep eutectics, the liquid phase is stabilized with respect to the crystalline solid, reducing the melting temperature, T_m, of the alloy. With a lower melting temperature, the temperature interval between the melting temperature and the glass transition temperature, T_g, is smaller. This temperature interval is the regime where nucleation and growth of a crystalline phase will occur; it must be bypassed without nucleation and growth of a crystalline phase to form a glass. A smaller interval between T_m and T_g reduces the time spent in this temperature interval (with a constant cooling rate), improving the glass-forming ability of the alloy. T_g varies relatively slowly with composition, so good metallic glass-forming alloys are found near deep eutectics [10].

Ti-Zr-Ni-Cu alloys are alloys that follow these rules for metallic glass formation. The Goldschmidt radii of the elements in this alloy are:

Ti	0.147 nm
Zr	0.160 nm
Ni	0.125 nm
Cu	0.128 nm

As evidenced in the Ti-Ni, Ti-Cu, Zr-Ni, and Zr-Cu binary phase diagrams [11] and in the Ti-Zr-Cu [12] and Ti-Zr-Ni [13] ternary phase diagrams, the elements in this alloy system also form deep eutectics. The glass-forming ability of this alloy system has been studied extensively [14, 15]. Two regions of the phase diagram with good glass-forming ability have been identified, a titanium rich region and a zirconium rich region. In between these two glass-forming regions lies an intermetallic phase. Finding a good glass-forming composition in this alloy system consisted of finding a deep eutectic that was removed from the intermetallic phase. The best quaternary glass former found is $Cu_{47}Ti_{34}Zr_{11}Ni_8$, lying in the titanium rich region. $Zr_{49}Cu_{33}Ti_{10}Ni_8$ is another good glass former, found in the zirconium rich region.

Compared to other metallic glass-forming compositions, $Cu_{47}Ti_{34}Zr_{11}Ni_8$ is a relatively good glass former, with a critical cooling rate of ~1000 K/s [16]. Although $Cu_{47}Ti_{34}Zr_{11}Ni_8$ is not as good a glass former as $Zr_{41.2}Ti_{13.8}Cu_{12.5}Ni_{10}Be_{22.5}$, one of the best metallic glass-forming alloys, it does have the advantage of not containing beryllium, thus making it safer to process and handle. As shown in Fig. 2, $Cu_{47}Ti_{34}Zr_{11}Ni_8$ is also unique in that it differs substantially in composition from other quaternary and quintary metallic glass-forming alloys. This thesis is a study of the thermophysical properties, crystallization, and the effect of small alloying additions on the thermal stability of the $Cu_{47}Ti_{34}Zr_{11}Ni_8$ glass-forming alloy.

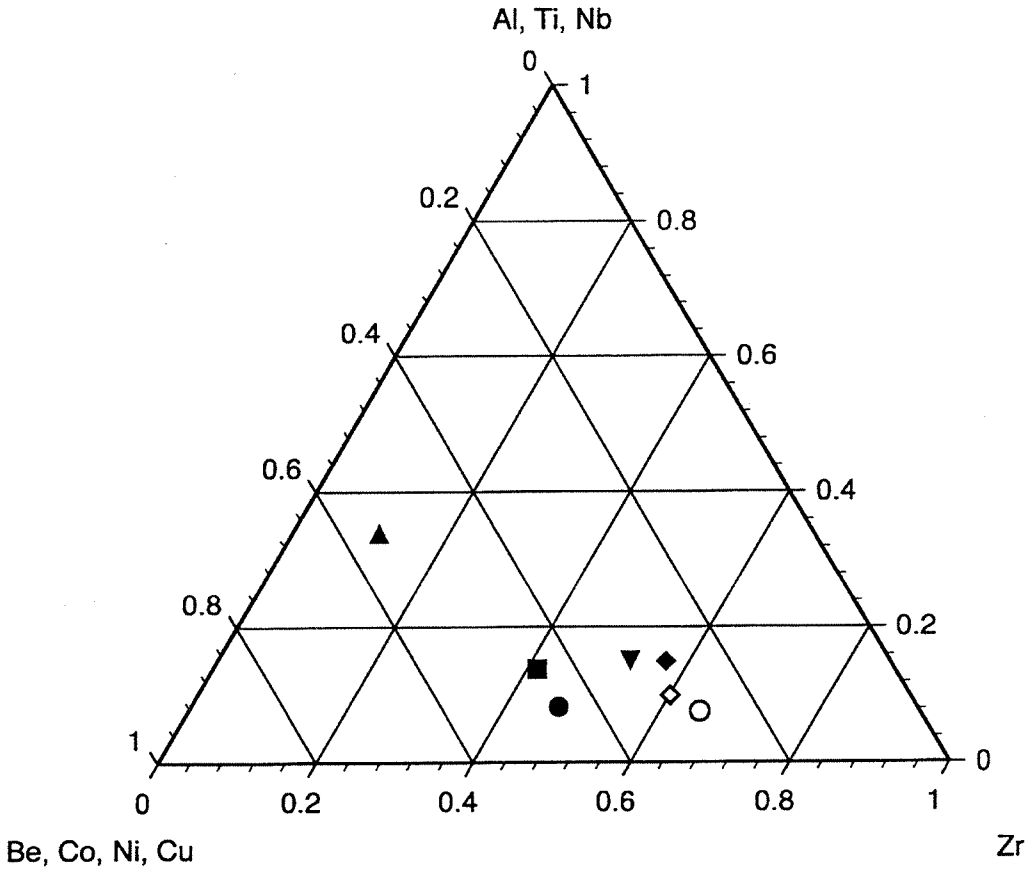

Fig. 2 $Cu_{47}Ti_{34}Zr_{11}Ni_8$ *and other metallic glass-forming alloys in a pseudo-ternary phase diagram*

The following metallic glass-forming alloys appear in the phase diagram: ▲ $Cu_{47}Ti_{34}Zr_{11}Ni_8$, ■ $Zr_{41.2}Ti_{13.8}Cu_{12.5}Ni_{10}Be_{22.5}$, ● $Zr_{46.75}Ti_{8.25}Cu_{7.5}Ni_{10}Be_{27.5}$, ▼ $Zr_{52.5}Cu_{17.9}Ni_{14.6}Al_{10}Ti_5$, ◆ $Zr_{57}Cu_{15.4}Ni_{12.6}Al_{10}Nb_5$, ○ $Zr_{65}Cu_{17.5}Al_{7.5}Ni_{10}$, *and* ◇ $Zr_{60}Cu_{18}Al_{10}Ni_9Co_3$. *In the center of the diagram is an approximate region where intermetallic phases are formed.*

The thermophysical properties of $Cu_{47}Ti_{34}Zr_{11}Ni_8$ that were measured are presented in chapter 2. Specific heat capacity data are presented in chapter 2.1, from which the differences in the thermodynamic functions between the liquid and the crystalline states were derived, chapter 2.2. Chapter 2.3 includes viscosity data for the alloy. These data show that the thermodynamics and the kinetics of $Cu_{47}Ti_{34}Zr_{11}Ni_8$ match empirical observations.

The results of the crystallization of $Cu_{47}Ti_{34}Zr_{11}Ni_8$ when it is annealed near the glass transition temperature are presented in chapter 3. Crystallization studies on metallic glass-forming alloys are important in investigating glass formation in these systems and also in possibly improving the glass-forming ability of an alloy.

Small additions of other elements have been found to improve the thermal stability of some metallic glass-forming alloys. Small additions of silicon to $Cu_{47}Ti_{34}Zr_{11}Ni_8$ improve both the thermal stability of the supercooled liquid against crystallization and the glass-forming ability of the alloy. In chapter 4.1, the results of a study on the effect of silicon in $Cu_{47}Ti_{34}Zr_{11}Ni_8$ with transmission electron microscopy and field ion microscopy/atom probe tomography are presented and discussed. Small magnesium and germanium additions were made to $Cu_{47}Ti_{34}Zr_{11}Ni_8$ to determine if these additions have a similar effect on the thermal stability as that of the silicon addition. These results are presented in chapter 4.2.

2. THERMOPHYSICAL PROPERTIES OF $Cu_{47}Ti_{34}Zr_{11}Ni_8$

Forming an amorphous solid via cooling from the liquid state involves a combination of thermodynamic and kinetic factors. The thermodynamic factors determine the driving force for crystallization, while the kinetic factors determine how quickly the nucleation and growth of a crystalline phase can occur. If the liquid is cooled to the glass transition temperature, the thermodynamic driving force for crystallization is still large. However, the kinetics of the system are so slow that the liquid will not crystallize; the kinetic barrier to forming the equilibrium phase is so large that the liquid configuration is trapped in the glassy state.

The thermodynamic and kinetic factors that are involved in nucleation are contained in classical nucleation theory. A liquid is not thermodynamically stable with respect to the crystalline phase below the melting temperature, T_m; i.e., the liquid state is not the lowest energy state below T_m. As a liquid is cooled below its melting temperature, the free energy change due to nucleation of a crystalline embryo of radius r is given by

$$\Delta G(r) = -\frac{4}{3}\pi\, r^3 \Delta G_v + 4\pi\, r^2 \gamma_{SL}, \qquad (1)$$

where ΔG_v is the free energy difference between the liquid and the solid per unit volume and γ_{SL} is the solid/liquid interfacial free energy. ΔG_v is the driving force for crystallization, which increases with increasing undercooling. The free energy barrier that must be overcome to form a stable nucleus is given by

$$\Delta G^* = \frac{16\pi}{3}\frac{\gamma_{SL}^3}{\Delta G_v^2}. \quad (2)$$

As the liquid is cooled below the melting temperature, this free energy barrier to nucleation decreases with increasing undercooling.

The steady-state nucleation rate, in a simple form, is given by

$$I_s = AD_{eff}\exp\left(-\frac{\Delta G^*}{k_B T}\right), \quad (3)$$

where D_{eff} is the effective diffusivity and A is a constant. The exponential term, where k_B is Boltzman's constant, gives the probability of forming a nucleus of critical size. The effective diffusivity is related to the viscosity of the system via the Stokes-Einstein relation [17]

$$D(T) = \frac{k_B T}{6\pi\left[\eta(T)\right]R}, \quad (4)$$

where $\eta(T)$ is the temperature dependent viscosity, and R is the radius of the diffusing particle. So, as the viscosity of a liquid increases with decreasing temperature, the nucleation rate decreases due to the lack of atomic mobility.

Although classical nucleation theory is only applicable in polymorphic crystallization, which is not the case for many metallic glass-forming systems, it does show how thermodynamic and kinetic factors are involved in nucleation. Since the nucleation of a crystalline phase must be avoided for glass formation, these thermodynamic and kinetic factors are important in studying glass formation in different systems.

Specific heat capacity data for $Cu_{47}Ti_{34}Zr_{11}Ni_8$ in both the liquid and the crystalline states are presented in chapter 2.1. Using these data, the differences in the thermodynamic functions between the liquid and the crystalline states of $Cu_{47}Ti_{34}Zr_{11}Ni_8$ were calculated, presented in chapter 2.2. The viscosity of $Cu_{47}Ti_{34}Zr_{11}Ni_8$ is presented in chapter 2.3.

2.1. Specific Heat Capacity

An alloy of nominal composition $Cu_{47}Ti_{34}Zr_{11}Ni_8$ was prepared in an arc melter with a titanium gettered, ultrahigh purity argon atmosphere, with elements of purities from 99.9% to 99.9999%. Ingots were flipped and remelted repeatedly to promote homogeneity. To obtain amorphous samples for differential scanning calorimetry (DSC) experiments, the alloy was remelted in a fused quartz tube in a high frequency induction furnace and then injection cast with ultrahigh purity argon into a copper mold. The molten metal was held in the quartz tube for as short a time as possible (usually < 10 seconds) to avoid any contamination.

To derive the thermodynamic functions for a system, the heat capacity of the system must be measured. Heat capacity is given by the ratio of the quantity of heat added to or withdrawn from a system to the resulting temperature change,

$$c = \frac{q}{\Delta T}. \tag{5}$$

Heat capacity is an extensive quantity, so it is usually expressed per unit quantity of the system being measured, the specific heat capacity. The heat capacity measured in this work is the heat capacity at constant pressure, c_p.

A differential scanning calorimeter (*Perkin Elmer DSC-7*) was used to determine the absolute specific heat capacity of the $Cu_{47}Ti_{34}Zr_{11}Ni_8$. Heating a sample at 0.333 K/s and then holding it at a constant temperature results in a step in heat flux given by

$$\dot{Q} = \frac{\partial Q}{\partial t} = \left(\frac{\partial Q}{\partial t}\right)_{\dot{T}\neq 0} - \left(\frac{\partial Q}{\partial t}\right)_{\dot{T}=0} = c \cdot \frac{dT}{dt}, \tag{6}$$

where $(\partial Q / \partial t)_{\dot{T}\neq 0}$ is the power required to heat the sample and sample pan at a constant heating rate, $(\partial Q / \partial t)_{\dot{T}=0}$ is the power needed to hold the sample and sample pan at a constant temperature, and c is the heat capacity of the sample and sample pan. By performing these heat flux steps every 20 K on the metal sample in the sample pan, a sapphire standard in the sample pan, and the sample pan by itself, the absolute specific heat capacity of the metal sample can be determined by

$$c_p(T)_{metal} = \frac{\dot{Q}_{metal} - \dot{Q}_{pan}}{\dot{Q}_{sapphire} - \dot{Q}_{pan}} \cdot \frac{m_{sapphire} \cdot \mu_{metal}}{m_{metal} \cdot \mu_{sapphire}} \cdot c_p(T)_{sapphire}, \tag{7}$$

where m_i is mass, μ_i is molar mass, and $c_p(T)_{sapphire}$ is the heat capacity of sapphire [18].

The absolute specific heat capacity of the supercooled liquid immediately after the glass transition could not be measured with the method described above because $Cu_{47}Ti_{34}Zr_{11}Ni_8$ is not very stable against crystallization in this temperature regime. To determine the specific heat capacity in this temperature range, constant heating rate DSC experiments were performed at 0.333, 0.667, 1.33, and 3.33 K/s. The specific heat capacity is determined by

$$c_{p,glass} = \frac{\dot{Q}\,\mu}{\dot{T}\,m} + c_{p,crystal} + scaling\ \ constant\,, \tag{8}$$

where $\dot{Q}$ is the power input, $\dot{T}$ is the heating rate, m is the mass, and μ is the molar mass. The DSC was calibrated for each heating rate to account for the shift in temperature with different heating rates.

Alternating current (ac) modulation calorimetry [19, 20] was used to measure the specific heat capacity of the equilibrium liquid. The ac modulation calorimetry technique was performed with TEMPUS (Tiegelfreies Elektromagnetisches Prozessieren Unter Schwerelosigkeit, see Refs. 21 and 22), an electromagnetic processing facility that flew on board the National Aeronautics and Space Administration's (NASA) space shuttle. ac modulation calorimetry is a noncontact technique which offers the advantages of possibly accessing the supercooled liquid state (due to a lack of heterogeneous nucleation sites) and of avoiding contamination of the chemically reactive molten metal sample from a container. Also, the TEMPUS facility can be operated under ultra-high vacuum, isolating the metallic melt from oxygen and other gaseous contaminants. With an electromagnetic processing facility, these ac modulation calorimetry experiments must be performed in a microgravity environment. On the ground, the heating due to the strong levitation forces needed to levitate a sample do not allow for lower sample temperatures; in a microgravity environment, a levitation force is not needed.

A diagram of the TEMPUS experimental facility is shown in Fig. 3. An electromagnetic quadrapole field was used to position the sample in the radio-frequency (rf) coils and an electromagnetic dipole field was used to heat the sample. A camera provided images for observation of the sample during the experiments and for thermal

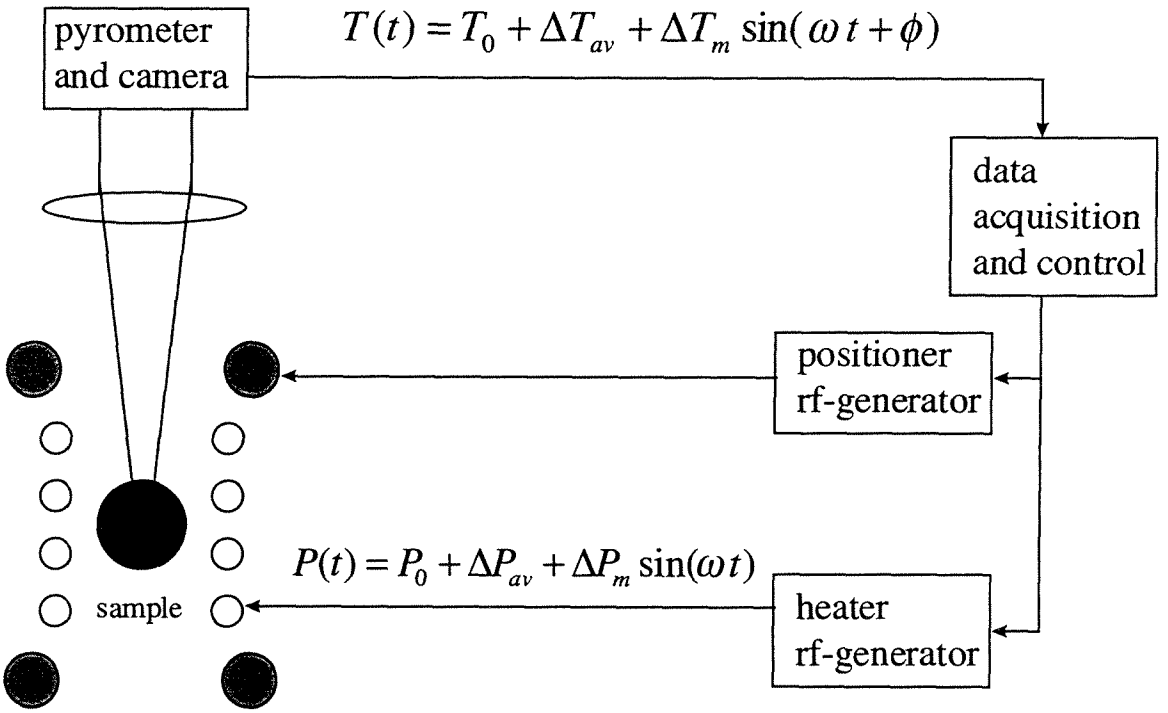

Fig. 3 Schematic diagram of the TEMPUS experimental facility

P(t) is the power input to the sample and T(t) is the resulting temperature response.

expansion coefficient, viscosity, and surface tension measurements. Measurements of sample temperature were made with a pyrometer.

By modulating the power input to the sample and measuring the temperature response, the heat capacity can be determined. Superimposing a voltage modulation, $U_m \sin(\omega t)$, on the constant voltage, U_0, of the heater rf circuit, results in a power modulation. The power input to the sample is proportional to $U(t)^2$, which is described by

$$P(t) = P_0 + \Delta P_{av} + \Delta P_m \sin(\omega t). \tag{9}$$

The power input to the sample is calibrated by performing modulations on the sample in the crystalline state, for which the heat capacity is known. This power modulation results in a temperature response of the sample described by

$$T(t) = T_0 + \Delta T_{av} + \Delta T_m \sin(\omega t + \phi), \tag{10}$$

where T_0 is the sample temperature before the modulations begin, ΔT_{av} is the increase in sample temperature, ΔT_m is the amplitude of the temperature modulation, ω is the modulation frequency, and ϕ is the phase shift in the temperature response from the power modulation.

Two time constants are important in this experimental method:

$$\tau_1 = \frac{c_p}{4A\varepsilon_T \sigma T_0^3} \tag{11}$$

and

$$\tau_2 = \frac{3c_p}{4\pi^3 R\kappa_{th}}, \tag{12}$$

where c_p is the sample heat capacity, A is the sample surface area, ε_T is the total hemispherical emissivity of the sample surface, σ is the Stefan-Boltzman constant, T_0 is the sample temperature, R is the sample radius, and κ_{th} is the sample thermal conductivity. τ_1 is the external relaxation time due to radiative heat loss and τ_2 is the internal relaxation time due to the finite thermal conductivity of the sample.

Heat capacity is determined by

$$c_p = f(\omega,\tau_1,\tau_2)\frac{\Delta P_m(\omega)}{\Delta T_m(\omega)\omega}, \tag{13}$$

where f is a correction function for radiation loss and finite thermal conductivity, $\Delta P_m(\omega)$ is the amplitude of the power modulation, $\Delta T_m(\omega)$ is the amplitude of temperature response to the power modulation, and ω is the modulation frequency. Due to the two time constants being well separated in time, there exists a modulation frequency range with $\omega\tau_2 \ll 1 \ll \omega\tau_1$, for which $f(\omega,\tau_1,\tau_2) \approx 1$. Modulation frequencies of 0.08 and 0.12 Hz were used in these experiments. An example of ac modulation calorimetry data collected with TEMPUS is shown in Fig. 4. In a typical experiment, the alloy was melted, overheated, and then cooled to a temperature where the modulations for the calorimetry were performed. Further details on these experiments can be found in Refs. 23-25.

To compare the thermodynamics of the liquid and the solid states, the heat of fusion must also be measured. A differential thermal analyzer (*Perkin Elmer DTA-7*),

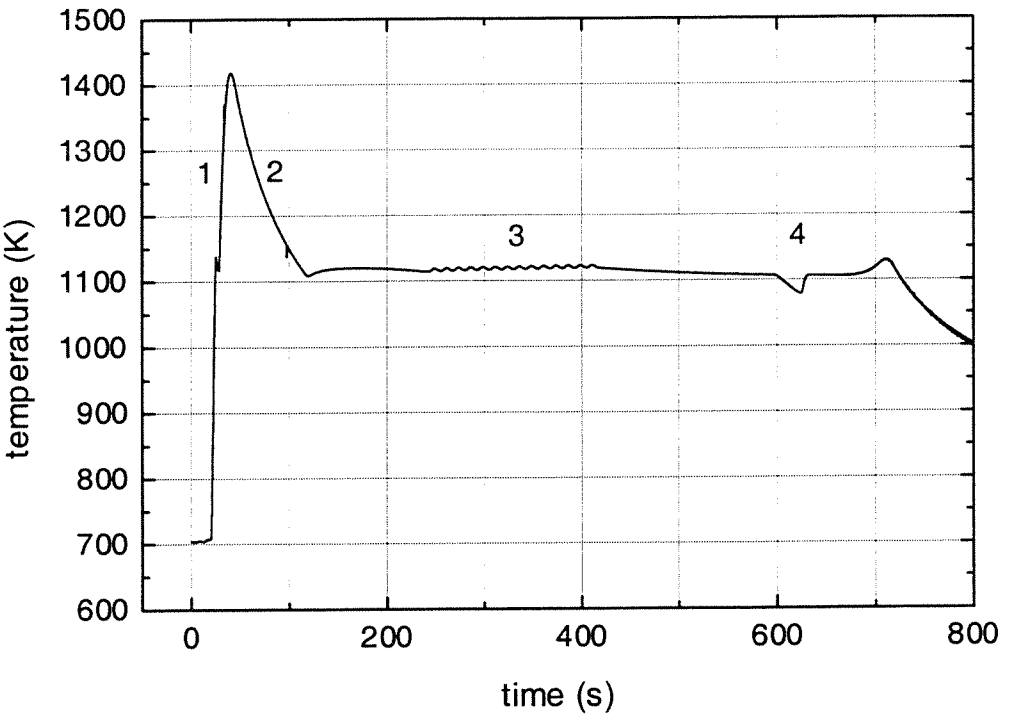

Fig. 4 A representative ac modulation calorimetry experiment

In the ac modulation calorimetry experiments, the alloy is melted, overheated (1), and cooled (2). ac modulations are then performed (3), after which the sample is further cooled, where it recalesces into a crystalline phase (4).

with a heating rate of 0.167 K/s, was used to determine the heat of fusion, the solidus temperature, and the liquidus temperature of $Cu_{47}Ti_{34}Zr_{11}Ni_8$. Graphite crucibles (*POCO DFP-1* graphite) were used in these experiments to minimize the reaction between the molten alloy and crucible.

Upon heating an amorphous alloy at a constant rate, the alloy goes through the glass transition, crystallizes, and then melts. This behavior is shown in Fig. 5, a differential scanning calorimeter scan and a differential thermal analyzer scan of $Cu_{47}Ti_{34}Zr_{11}Ni_8$. The onset of the glass transition, T_g, is indicated by a small endothermic rise. T_g = 673 K at a heating rate of 0.333 K/s. Crystallization begins at T_x = 717 K, with three exothermic peaks. These three exothermic peaks are due to the crystallization of different phases (discussed in chapter 3). Melting begins at the solidus temperature of $T_{solidus}$ = 1114 K, with the alloy being completely molten at the liquidus temperature of $T_{liquidus}$ = 1128 K. The heat of fusion is 11.3 kJ g-atom^{-1}, found by integrating the area of the melting endotherm.

The specific heat capacity of $Cu_{47}Ti_{34}Zr_{11}Ni_8$ in the crystalline solid, the amorphous solid, the supercooled liquid, and the equilibrium liquid is shown in Fig. 6. The specific heat capacity for the crystalline and the amorphous states was determined by DSC experiments, while the specific heat capacity of the equilibrium liquid was determined by ac modulation calorimetry. The crystalline state of this alloy is not well characterized, and consists of multiple phases. Also, since the amorphous solid is not in thermodynamic or metastable equilibrium in the glass transition region, heat capacity data in this region are not included.

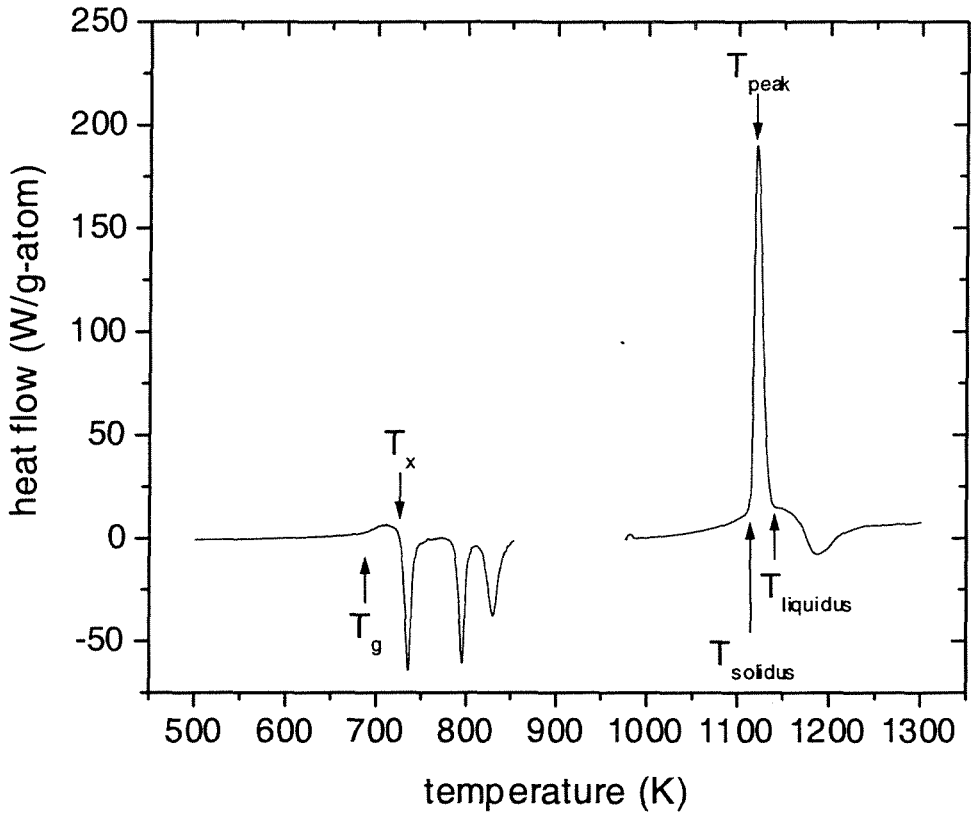

Fig. 5 Thermal behavior of $Cu_{47}Ti_{34}Zr_{11}Ni_8$ upon heating

The lower temperature data were obtained with a DSC (heating rate of 0.333 K/s) and the higher temperature data were obtained with a DTA (heating rate of 0.167 K/s). The onset of the glass transition, T_g, the onset of crystallization, T_x, the solidus temperature, $T_{solidus}$, the temperature at the peak of the melting endotherm, T_{peak}, and the liquidus temperature, $T_{liquidus}$, are indicated. The exothermic hump after the melting peak is due to the reaction of the alloy with the graphite crucible.

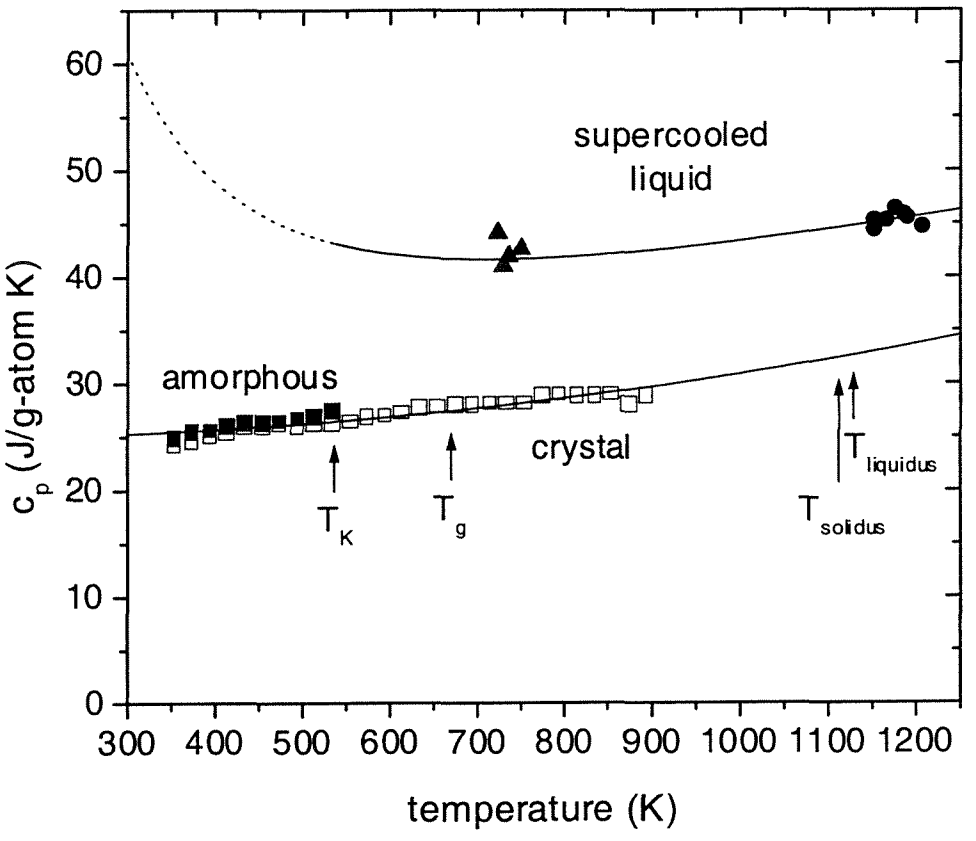

Fig. 6 Specific heat capacity of $Cu_{47}Ti_{34}Zr_{11}Ni_8$

The specific heat capacity of $Cu_{47}Ti_{34}Zr_{11}Ni_8$ in the crystalline solid (□), the amorphous alloy (■), the supercooled liquid measured with constant heating rate experiments (▲), and the equilibrium liquid measured with ac modulation calorimetry (●). The lines on the graphs are the fits to Equations (14) and (15). Also indicated on this plot are the Kauzmann temperature, T_K, the glass transition temperature, T_g (onset with a heating rate of 0.333 K/s), the solidus temperature, $T_{solidus}$, and the liquidus temperature, $T_{liquidus}$.

The heat capacity of a crystal well above the Debye temperature can be described by [26]

$$c_{p,crystal}(T) = 3R + a \cdot T + b \cdot T^2 . \quad (14)$$

The heat capacity of an undercooled liquid can be described by

$$c_{p,liquid}(T) = 3R + c \cdot T + d \cdot T^{-2} . \quad (15)$$

R = 8.31452 J g-atom^{-1}K^{-1}, and a, b, c, and d are fitting constants. The fitting constants for the heat capacity data are a = -0.00089 J g-atom^{-1} K^{-2}, b = 6.82×10^{-6} J g-atom^{-1} K^{-3}, c = 0.0156 J g-atom^{-1} K^{-2}, and d = 2.83×10^{6} J g-atom^{-1} K.

2.2. Thermodynamics

The difference in the specific heat capacity between the liquid and the crystalline states, Δc_p^{l-x}, was calculated. With these data, the differences in the thermodynamic functions between the liquid and the crystalline states were determined. The calculated difference in enthalpy is given by

$$\Delta H^{l-x}(T) = \Delta H_f - \int_T^{T_f} \Delta c_p^{l-x}(T')dT' \quad (16)$$

and is shown in Fig. 7. In this equation, ΔH_f is the enthalpy of fusion and T_f is the temperature at which the Gibbs free energy values of the liquid and the crystalline states are taken to be equal. The difference in the enthalpy between the liquid and the crystalline states at the glass transition (measured with a rate of 0.333 K/s) is the amount of enthalpy frozen into the liquid at T_g.

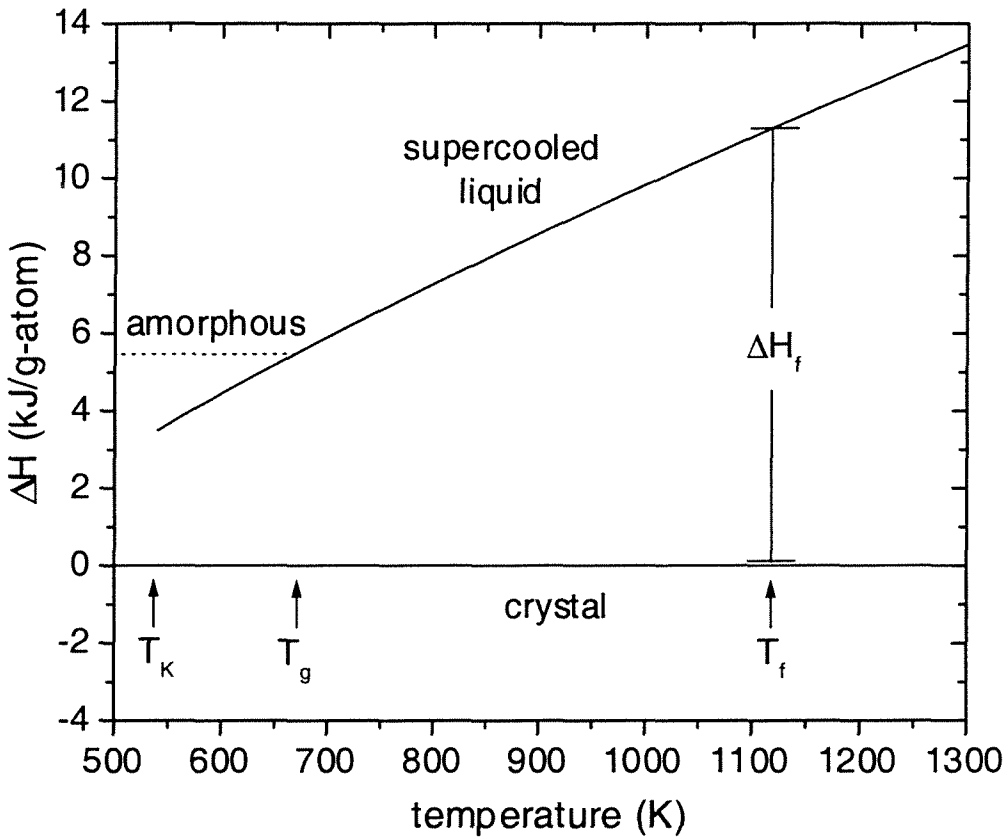

Fig. 7 Enthalpy difference between the liquid and crystalline states of $Cu_{47}Ti_{34}Zr_{11}Ni_8$

The calculated difference in enthalpy between the liquid and the crystalline states of $Cu_{47}Ti_{34}Zr_{11}Ni_8$. *Also indicated on this plot are the Kauzmann temperature,* T_K, *the glass transition temperature,* T_g *(onset with a heating rate of 0.333 K/s), and the temperature at which the Gibbs free energy values of the liquid and the crystalline states are taken to be equal,* T_f.

T_f, the temperature at which the Gibbs free energy values of the liquid and the crystalline states are taken to be equal, is not known exactly for $Cu_{47}Ti_{34}Zr_{11}Ni_8$. However, the Gibbs free energy of the liquid state equals the Gibbs free energy of the crystalline state between the solidus and liquidus temperatures. T_f was taken to be the temperature at which the endothermic peak is maximum during melting (determined with the DTA), T_{peak}, which is 1119 K for $Cu_{47}Ti_{34}Zr_{11}Ni_8$.

The calculated difference in entropy between the liquid and crystalline states is given by

$$\Delta S^{l-x}(T) = \Delta S_f - \int_T^{T_f} \frac{\Delta c_p^{l-x}(T')}{T'} dT' \tag{17}$$

and is shown in Fig. 8. ΔS_f, the entropy of fusion, is given by

$$\Delta S_f = \frac{\Delta H_f}{T_f}. \tag{18}$$

The entropy of fusion for $Cu_{47}Ti_{34}Zr_{11}Ni_8$ is 10.1 J g-atom^{-1} K^{-1}. T_{peak} is used in place of T_f in this calculation. Similar to the $\Delta H^{l-x}(T)$ function that was calculated, there is residual entropy frozen into the glass below the glass transition temperature.

The T_K indicated on these plots is the calculated Kauzmann temperature. The Kauzmann temperature is the isentropic temperature, the temperature at which the configurational entropy of the liquid is equal to the configurational entropy of the crystal. This temperature is commonly believed to be the lowest temperature at which a supercooled liquid can exist without either spontaneously crystallizing or forming a glass [27]. The calculated Kauzmann temperature for $Cu_{47}Ti_{34}Zr_{11}Ni_8$ is 537 K. It is important

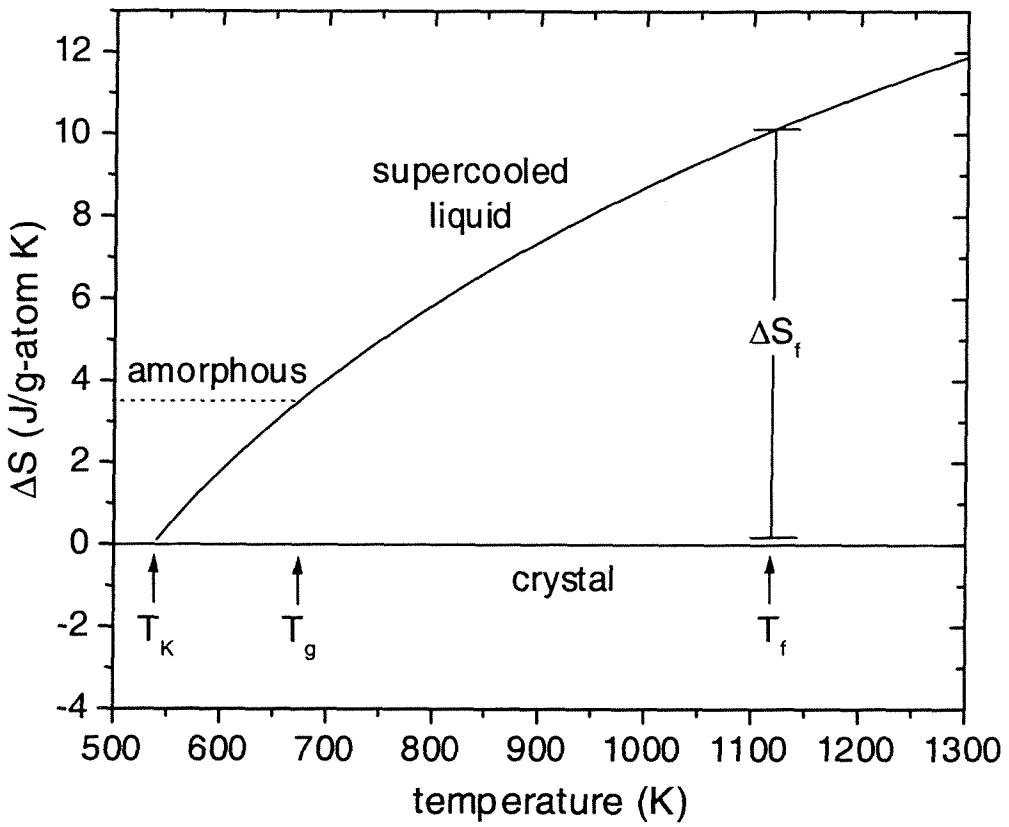

Fig. 8 Entropy difference between the liquid and crystalline states of $Cu_{47}Ti_{34}Zr_{11}Ni_8$

The calculated difference in entropy between the liquid and the crystalline states of $Cu_{47}Ti_{34}Zr_{11}Ni_8$. *Indicated on this plot are the Kauzmann temperature,* T_K, *the glass transition temperature,* T_g *(onset with a heating rate of 0.333 K/s), and the temperature at which the Gibbs free energy values of the liquid and the crystalline states are taken to be equal,* T_f.

to note that the entropy difference that is calculated from the heat capacity data is the total entropy difference between the liquid and the crystalline states and not the configurational entropy difference. The total entropy difference between the liquid and the crystalline states includes configurational entropy and vibrational entropy. Thus, this calculated Kauzmann temperature does not necessarily represent the temperature where the configurational entropy of the liquid equals the configurational entropy of the crystal.

The calculated difference in the Gibbs free energy between the liquid and crystalline states is given by

$$\Delta G^{l-x}(T) = \left(\Delta H_f - \int_T^{T_f} \Delta c_p^{l-x}(T')dT' \right) - T\left(\Delta S_f - \int_T^{T_f} \frac{\Delta c_p^{l-x}(T')}{T'} dT' \right) \qquad (19)$$

and is shown in Fig. 9.

A comparison of the Gibbs free energy difference between the liquid and the crystalline states for several metallic glass-forming alloys [18, 28] is shown in Fig. 10, along with the estimated critical cooling rates for these alloys. In general, the lower the Gibbs free energy difference between the liquid and the crystalline states, the better the glass-forming ability of the alloy according to the critical cooling rate. It is important to note that this Gibbs free energy difference is the driving force for crystallization only in the case of a polymorphic transformation. If the crystallization is not polymorphic, as is the case for many metallic glass-forming compositions, this free energy difference is the lower limit of the thermodynamic driving force for crystallization.

Also, in general, the smaller the entropy of fusion, the better the glass-forming ability of the metallic glass-forming alloys. This can be understood by the Turnbull approximation [29],

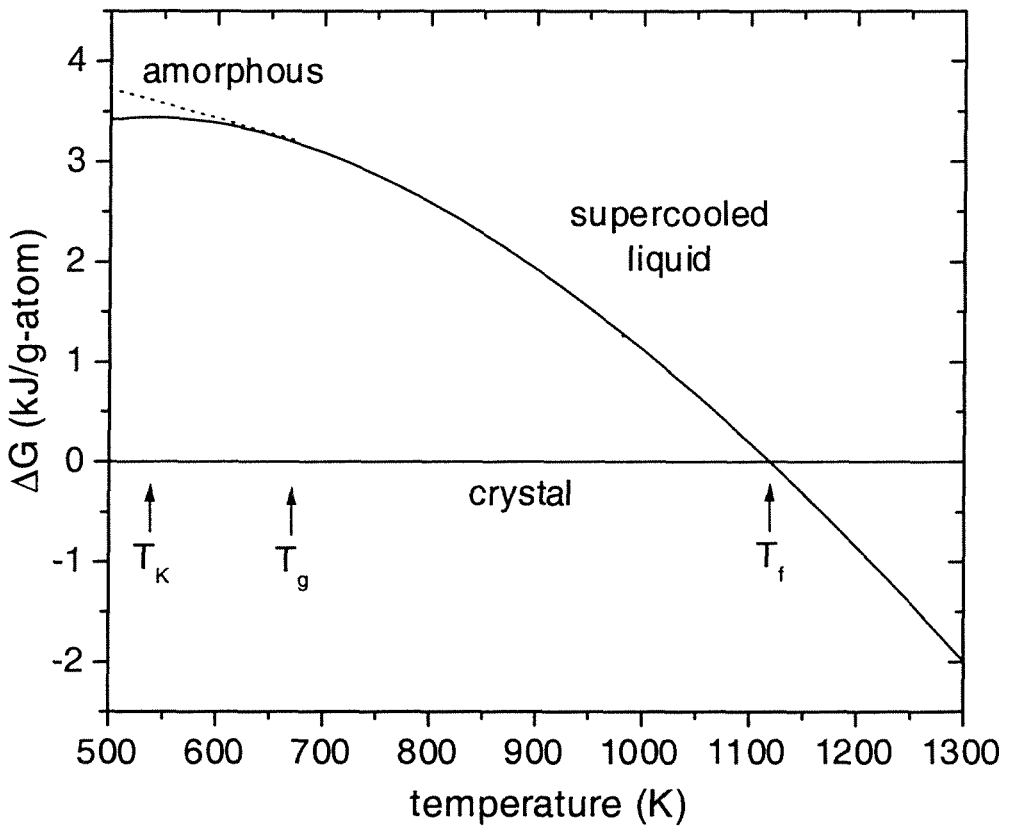

Fig. 9 Gibbs free energy difference between the liquid and crystalline states of $Cu_{47}Ti_{34}Zr_{11}Ni_8$

The calculated difference in the Gibbs free energy between the liquid and the crystalline states of $Cu_{47}Ti_{34}Zr_{11}Ni_8$*. Also indicated on this plot are the Kauzmann temperature,* T_K*, the glass transition temperature,* T_g *(onset with a heating rate of 0.333 K/s), and the temperature at which the Gibbs free energy values of the liquid and the crystalline states are taken to be equal,* T_f*.*

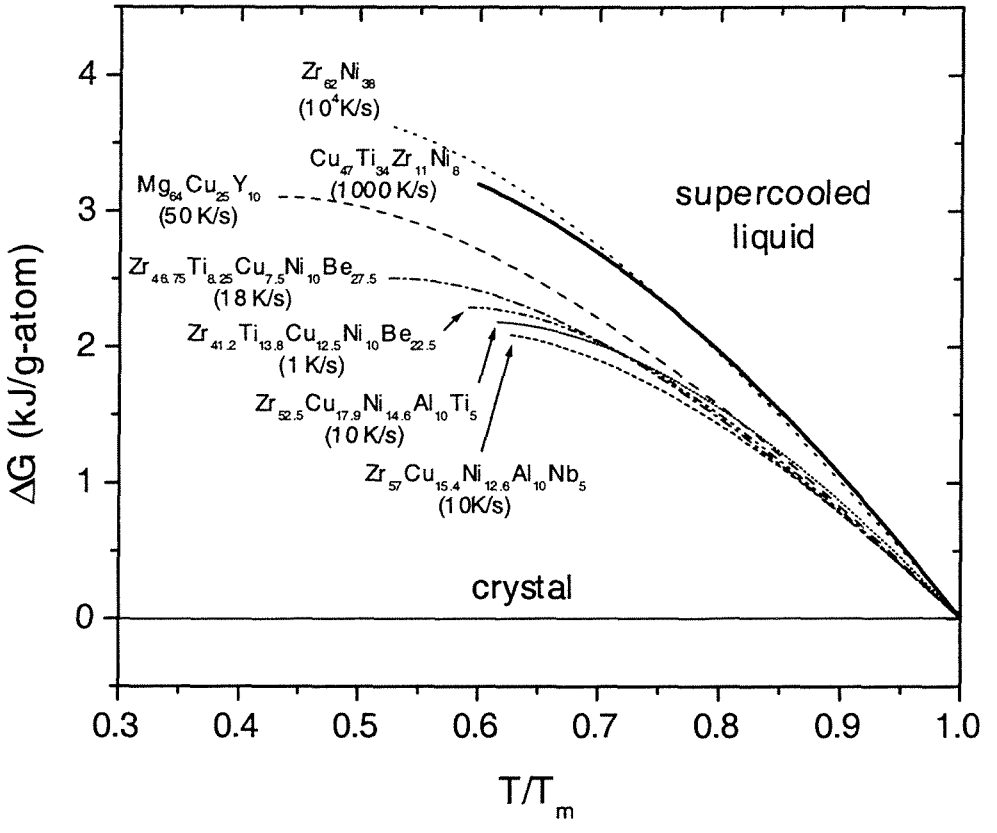

Fig. 10 Gibbs free energy difference between the liquid and crystalline states for a number of metallic glass-forming alloys

These data have been normalized by the melting temperatures of the alloys. For $Cu_{47}Ti_{34}Zr_{11}Ni_8$, the melting temperature is taken as T_f. Also listed for these alloys is the critical cooling rate for glass formation. Data for the other alloys were taken from Refs. 18 and 28.

$$\Delta G^{l-x} = \Delta H_f - T\Delta S_f \,, \tag{20}$$

which is a good approximation immediately below the melting point. Initially, as the liquid is undercooled, the entropy of fusion, ΔS_f, determines the rate at which ΔG^{l-x} changes.

Another parameter that is an indicator of the glass-forming ability in glass-forming alloys is the reduced glass transition temperature, T_{rg} [30]. The reduced glass transition temperature is given by

$$T_{rg} = \frac{T_g}{T_m}, \tag{21}$$

where T_g is the glass transition temperature and T_m is the melting temperature. This quantity is derived from Turnbull's classical theory of nucleation and growth of crystalline phases in an undercooled liquid [29]. It is a measure of the time spent in the supercooled liquid regime when cooling the liquid from the melt. Larger reduced glass transition temperatures indicate better glass-forming ability; the temperature interval between the melting temperature and glass transition temperature is smaller, decreasing the likelihood of crystallization. T_{rg} for $Cu_{47}Ti_{34}Zr_{11}Ni_8$ (determined using the onset of the glass transition measured with a heating rate of 0.333 K/s and the liquidus temperature measured with a heating rate of 0.167 K/s) is 0.60. Values of the critical cooling rates and T_{rg} for $Cu_{47}Ti_{34}Zr_{11}Ni_8$ and some other metallic glass-forming alloys are given in Table I.

	critical cooling rate (K/s)	T_{rg}
$Zr_{41.2}Ti_{13.8}Cu_{12.5}Ni_{10}Be_{22.5}$ [31]	1	0.67
$Zr_{57}Cu_{15.4}Ni_{12.6}Al_{10}Nb_5$ [28]	10	0.62
$Zr_{52.5}Cu_{17.9}Ni_{14.6}Al_{10}Ti_5$	10	0.62
$Mg_{65}Cu_{25}Y_{10}$ [18]	50	0.59
$Cu_{47}Ti_{34}Zr_{11}Ni_8$	1000	0.60

Table I Critical cooling rates and reduced glass transition temperatures of selected metallic glass-forming alloys

2.3. Viscosity

As a liquid is cooled below its melting point, if nucleation and growth of crystalline phases are avoided, the viscosity of the liquid increases until the liquid is frozen in a solid form, i.e., a glass. Viscosity varies over many orders of magnitude for different liquids. The viscosities, in units of Pa s, of some common substances at room temperature are: air, 10^{-5}; water, 10^{-3}; honey, 10^{1}; and asphalt, 10^{8} [32]. A liquid is commonly considered to become a solid at a viscosity of 10^{12} Pa s. Viscosity is linked to atomic diffusivity via the Stokes-Einstein relation (Eq. (4)). Measurements of viscosity thus yield information about the kinetics of a system.

The viscosity of the amorphous solid and the supercooled liquid was measured by three-point beam bending experiments with a thermomechanical analyzer (*Perkin-Elmer TMA-7*). An alloy of nominal composition $Cu_{47}Ti_{34}Zr_{11}Ni_8$ was prepared for these experiments in an arc melter with a titanium gettered, ultrahigh purity argon atmosphere,

with elements of purities from 99.9% to 99.9999%. Ingots were flipped and remelted repeatedly to promote homogeneity. To obtain amorphous samples for the beam bending experiments, the alloy was remelted in a fused quartz tube with a high frequency induction furnace and then injection cast with ultrahigh purity argon into a copper mold with dimensions 1 × 4 × ~25 mm (thickness by width by length). Beams for the beam bending experiments were made by cutting the 1 mm thick amorphous strip on a diamond saw. The beams had cross-sectional areas ranging from 0.25 to 0.80 mm^2.

In the three-point beam bending experiments, a constant load was applied to the center of a beam of uniform cross section that was supported on its ends. Heating the sample (at a heating rate of 1.667 K/s to 623 K and then at a heating rate of 0.833 K/s to the desired temperature) and holding it isothermally resulted in a deflection of the center of the beam. Viscosity (in Pa s) at a given temperature is given by the equation [33, 34, 35]

$$\eta = \frac{gL^3}{144 I_c v}\left(M + \frac{5\rho AL}{8}\right), \tag{22}$$

where g is the gravitational constant (m/s^2), L is the support span length (5.08×10^{-3} m in these experiments), I_c is the cross-sectional moment of inertia (m^4, $I_c = (w \cdot h^3)/12$ with width w and height h for a rectangular beam), v is the midpoint deflection rate (m/s), M is the applied load (kg), ρ is the density of the sample (kg/m^3), and A is the cross-sectional area (m^2). Loads ranging from 100 mN to 900 mN were used in these experiments. This method can be used to measure viscosities ranging from 10^7 to 10^{14} Pa s.

For the three-point beam bending experiments, the samples were annealed until equilibrium was reached. The data can be fit to a stretched exponential relaxation function

$$\eta(t) = \eta_a + \eta_{eq}\left(1 - e^{-(t/\tau)^{\beta}}\right), \tag{23}$$

where η_a is the viscosity of the amorphous alloy before relaxation, η_{eq} is the equilibrium viscosity, t is time, τ is the average shear flow relaxation time, and β is a stretching exponent. The equilibrium viscosity, when measured on a long time scale, is equivalent to the viscosity of the supercooled liquid [36].

Viscosity measurements in the equilibrium liquid were made for $Cu_{47}Ti_{34}Zr_{11}Ni_8$ with a noncontact oscillating drop technique [37]. A noncontact technique offers the advantages of possibly being able to access the supercooled liquid regime and of avoiding contamination of the sample. These measurements were made under microgravity conditions with TEMPUS. By measuring the damping of oscillations of the spherical sample, the viscosity can be determined for the fundamental surface oscillation mode n = 2 by

$$\eta = \frac{3\ m\Gamma}{20\pi\ R_0}, \tag{24}$$

where m is the sample mass, Γ is the damping constant, and R_0 is the unperturbed sample radius.

The viscosity data for $Cu_{47}Ti_{34}Zr_{11}Ni_8$ are plotted in an Arrhenius plot in Fig. 11. Viscosity could not be measured at higher temperatures with the three-point beam bending experiments due to crystallization of the sample. These data are fit with a

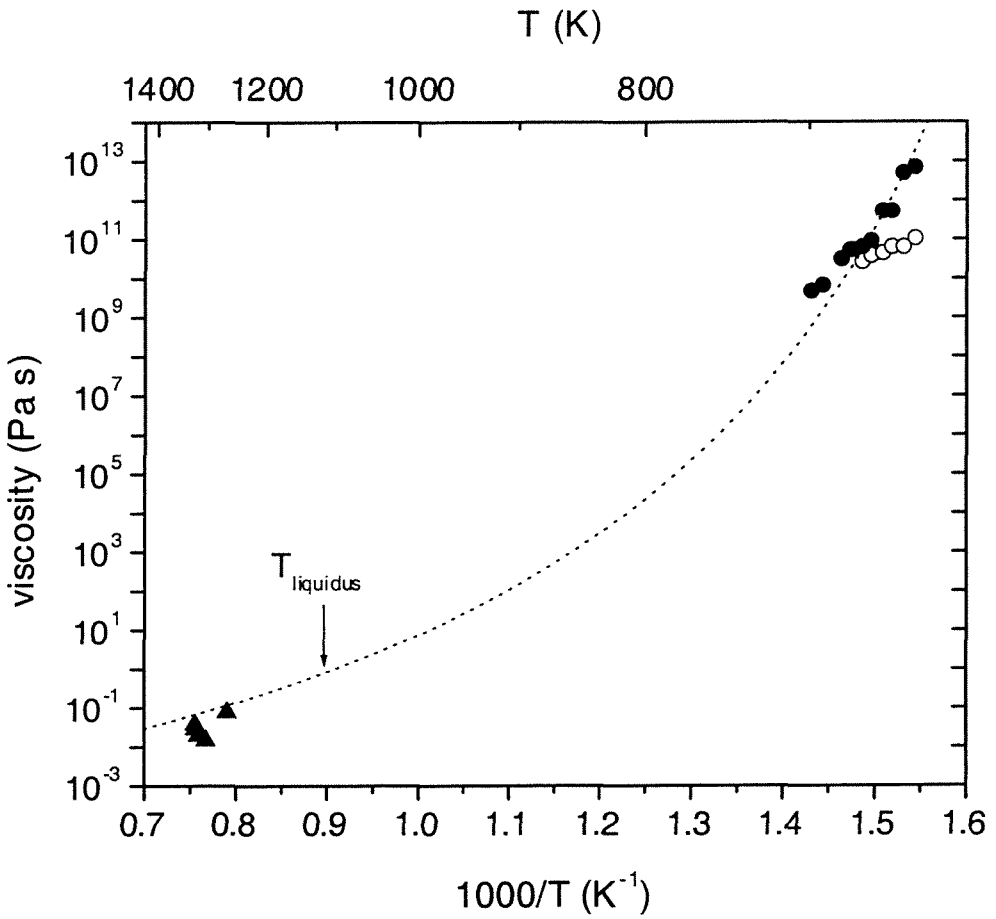

Fig. 11 Arrhenius plot of the viscosity of $Cu_{47}Ti_{34}Zr_{11}Ni_8$

Lower temperature viscosity of the amorphous solid and the supercooled liquid, both before reaching equilibrium (○) and after reaching equilibrium (●), was measured with three-point beam bending experiments. Higher temperature viscosity was measured with the non-contact oscillating drop technique (▲). The equilibrium data are fit with the VFT relation (dotted line), Eq. (25).

Vogel-Fulcher-Tammann (VFT) relation [38, 39, 40], an empirical equation that has been shown to fit the temperature dependence of viscosity over many orders of magnitude for glass-forming liquids [41]. The VFT relation, in a modified form [42], is

$$\eta = \eta_0 \cdot \exp\left(\frac{D^* \cdot T_0}{T - T_0}\right), \tag{25}$$

where D^* is the fragility parameter and T_0 is the VFT temperature (the temperature at which the barriers with respect to flow go to infinity). η_0 is the high temperature limit of viscosity, determined according to the relationship [43]

$$\eta_0 = h / V_a . \tag{26}$$

In this relation, h is Planck's constant, and V_a is the atomic volume of the liquid. $V_a = M/(N_A \rho)$, where M is the molar mass (60.87 g/g-atom), N_A is Avogadro's number, and ρ is the density of the liquid (~6 g/cm^3). This gives a value for η_0 of 4×10^{-5} Pa s. A fit of the data with the VFT equation yields $D^* = 12.0$ and $T_0 = 500$ K.

For some liquids, such as silicate glasses, the viscosity of the liquid follows an Arrhenius behavior; these liquids are called 'strong' liquids. Other liquids, such as organic and ionic glasses, show a non-Arrhenius behavior of viscosity; these liquids are called 'fragile' liquids. Angell [42] popularized this classification of strong and fragile liquids. When the viscosity data are fit with the VFT relation, strong liquids have fragility parameters, D^*, as high as 100, while fragile liquids have fragility parameters as low as 2. The fragility parameter of $Cu_{47}Ti_{34}Zr_{11}Ni_8$ is 12.0. A comparison of strong and fragile glass formers is in Fig. 12, an Arrhenius plot scaled by the glass transition

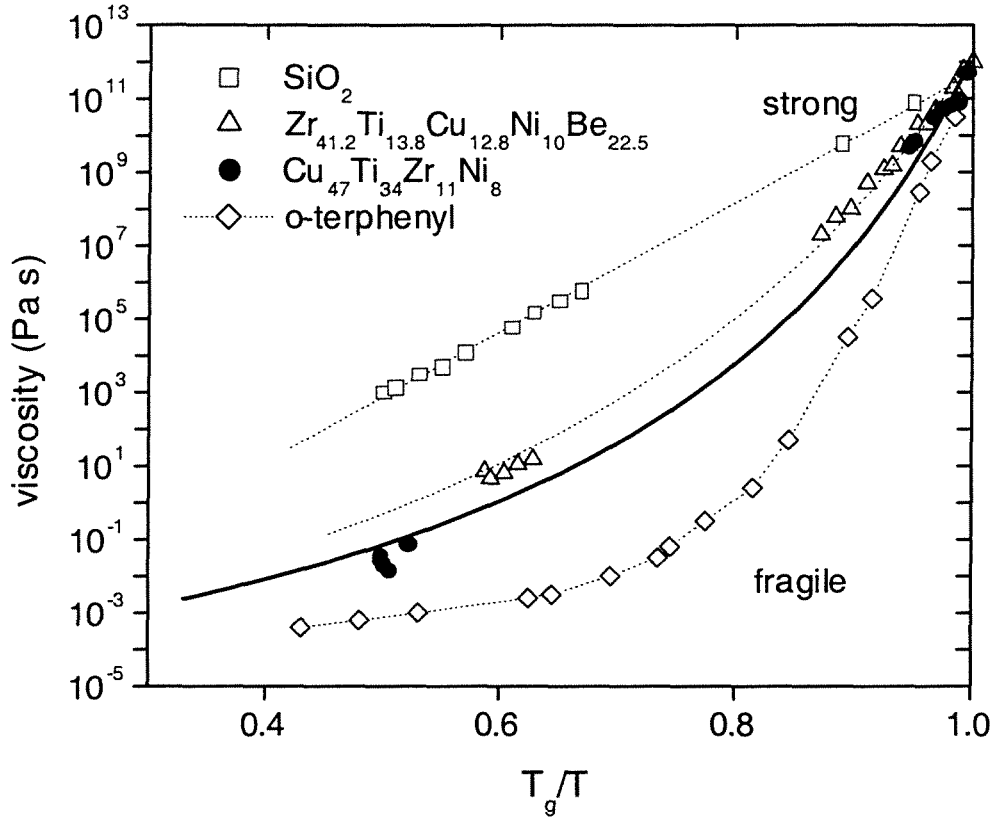

Fig. 12 Arrhenius plot of viscosity data for a number of glass formers

The viscosity data are scaled by the glass transition temperature, T_g. T_g is taken to be the temperature at which the viscosity is 10^{12} Pa s, commonly regarded as the viscosity at which a liquid becomes a solid. SiO_2 shows strong liquid behavior while o-terphenyl shows fragile liquid behavior. $Cu_{47}Ti_{34}Zr_{11}Ni_8$ is more fragile than one of the best metallic glass formers, $Zr_{41.2}Ti_{13.8}Cu_{12.8}Ni_{10}Be_{22.5}$. Data for the other glass formers in this plot were taken from Ref. 44.

temperature, T_g, of each material. T_g is taken as the temperature at which the viscosity has a value 10^{12} Pa s.

The fragility parameter, for materials of similar types (silicates, polymers, metals, etc.), is also a good indicator of the glass-forming ability of a material. In general, the larger the fragility parameter, the better the glass-forming ability of the liquid. Glasses with large fragility parameters have sluggish kinetics in the supercooled liquid regime, inhibiting crystallization of the liquid. A comparison of the critical cooling rates for glass formation and the fragility parameters of a number of metallic glass-forming alloys is given in Table II. These data were taken from Refs. 44 and 45.

	critical cooling rate (K/s)	D^*
$Zr_{46.75}Ti_{8.25}Cu_{7.5}Ni_{10}Be_{27.5}$	18 [46]	22.7
$Zr_{41.2}Ti_{13.8}Cu_{12.8}Ni_{10}Be_{22.5}$	1	18.5
$Pd_{48}Ni_{32}P_{20}$	<10	16.6
$Cu_{47}Ti_{34}Zr_{11}Ni_8$	1000	12.0
$Pd_{77.5}Cu_6Si_{16.5}$	500	11.1
$Au_{77.8}Ge_{13.8}Si_{8.4}$	$\sim 10^5$	8.4

Table II Critical cooling rates and fragility parameters, D^*, of selected metallic glass-forming alloys

3. CRYSTALLIZATION OF AMORPHOUS $Cu_{47}Ti_{34}Zr_{11}Ni_8$

Instead of polymorphically crystallizing, many metallic glass-forming alloys phase separate prior to crystallization [47]. This can be explained in terms of the confusion principle [9]. As discussed in chapter 1, metallic glass-forming alloys usually consist of three or more elements with the atomic sizes of the elements differing by at least 12%. As a result, crystalline phases which form from the molten alloy tend to be more complex than body centered cubic (bcc), face centered cubic (fcc), and hexagonal close packed (hcp) phases. However, as a way of escaping a chemically 'frustrated' composition, the alloy can phase separate into two liquids of differing compositions; nucleation may be favored in one of these new liquid compositions. This is another factor contributing to the good glass-forming ability of new metallic glass-forming alloys; phase separation prior to crystallization increases the time it takes for an alloy to crystallize.

When metallic glass-forming alloys crystallize at lower temperatures near the glass transition temperature, classical nucleation theory predicts few nuclei forming, resulting in a coarse microstructure. However, in many metallic glass-forming alloys, including $Zr_{41.2}Ti_{13.8}Cu_{12.5}Ni_{10}Be_{22.5}$ [48, 49], $Mg_{62}Cu_{25}Y_{10}Li_3$ [50], $Zr_{52.5}Cu_{17.9}Ni_{14.6}Al_{10}Ti_5$, and $Zr_{57}Cu_{15.4}Ni_{12.6}Al_{10}Nb_5$ [51], a fine microstructure of nanocrystals embedded in an amorphous matrix is observed. Different models have been proposed to account for this observed microstructure [52, 53, 54, 55].

In making a metallic glass, glass formation is equivalent to avoiding the nucleation and growth of crystalline phases when cooling the alloy from the molten liquid. Hence, studies on the crystallization processes of metallic glass-forming alloys are

important in understanding glass formation in metallic systems. This knowledge may also aid in the development of better metallic glass-forming alloys; if the crystallization process is understood, metallic glass-forming alloys could be designed that further frustrate the crystallization process, improving the glass-forming ability of the alloy.

In this chapter, the results of a study on the crystallization of amorphous $Cu_{47}Ti_{34}Zr_{11}Ni_8$ are presented. A number of different experimental techniques were used in this study, including differential scanning calorimetry (DSC), transmission electron microscopy (TEM), X-ray diffraction (XRD), field ion microscopy (FIM), atom probe tomography (APT), and small-angle neutron scattering (SANS). Atom probe tomography has a high spatial resolution, useful for detecting and characterizing ultrafine scale inhomogeneities due to phase separation, precipitation, clustering, or chemical short range ordering.

$Cu_{47}Ti_{34}Zr_{11}Ni_8$ phase separates into copper-enriched and titanium-enriched regions (the copper-enriched regions are low in titanium content and vice versa) before a crystalline phase nucleates and grows in the amorphous matrix. The primary nucleating phase has a face centered cubic structure.

3.1. Crystallization: Experimental

An alloy of nominal composition $Cu_{47}Ti_{34}Zr_{11}Ni_8$ was prepared in an arc melter with a titanium gettered, ultrahigh purity argon atmosphere, with elements of purities from 99.9% to 99.9999%. Ingots were flipped and melted repeatedly to promote homogeneity. To obtain amorphous samples, the alloy was remelted in a fused quartz

tube in a high frequency induction furnace and then injection cast with ultrahigh purity argon into a copper mold.

A differential scanning calorimeter (*Perkin Elmer DSC-7*) was used to study the thermal behavior of $Cu_{47}Ti_{34}Zr_{11}Ni_8$. In isothermal experiments with the DSC, the amorphous solid was heated to different temperatures near the glass transition temperature and held isothermally; the DSC was calibrated at 0.0167 K/s for these experiments. DSC scans (heating rate of 0.333 K/s) were also performed on samples of $Cu_{47}Ti_{34}Zr_{11}Ni_8$ that were heat-treated and isothermally annealed under various conditions. Isothermal anneals were performed by sealing a sample wrapped in tantalum foil in a quartz tube evacuated to a vacuum of 5×10^{-6} mbar or lower and placing this sample in an electric furnace.

Transmission electron microscopy (TEM) was performed on some of the heat-treated and isothermally annealed samples with a *Phillips EM430* operating at 300 kV with a lanthanum hexaboride (LaB_6) electron source. All samples were prepared by ultramicrotomy.

Field ion microscopy (FIM) and atom probe tomography (APT) specimens were prepared by casting the alloy in a copper mold of dimensions $1 \times 4 \times \sim25$ mm (thickness by width by length). Bars of cross section ~0.15 to 0.30 mm square were cut with a diamond saw. The bars were electropolished using 12.5% sulfuric acid in methanol (~9-14 V). Some bars were subsequently electropolished with a solution of 2% perchloric acid in 2-butoxyethanol (~9 V). Two different samples of $Cu_{47}Ti_{34}Zr_{11}Ni_8$ were characterized with FIM/APT: as-prepared and isothermally annealed (701 K for 24 h). The FIM/APT experiments were performed with an Energy-Compensated Optical

Position-Sensitive Atom Probe (ECOPoSAP) at Oak Ridge National Laboratory. Neon was used as the imaging gas for the field ion microscopy, with a sample temperature of 60 K. For the atom probe tomography, the pulse fraction was 20% of the standing voltage and the pulse repetition rate was 1500 Hz.

Small-angle neutron scattering (SANS) experiments were performed at the Intense Pulsed Neutron Source (IPNS) at Argonne National Laboratory with the small-angle neutron diffractometer (SAND) [56]. SANS data is taken in a Q region of 0.04 to 6 nm^{-1} ($Q = 4\pi \sin\theta / \lambda$, where θ is half the scatting angle and λ is the wavelength of the neutrons) in a single measurement using neutrons of wavelengths λ = 0.1 to 1.4 nm simultaneously in a time-of-flight mode. Samples for these experiments were prepared by injection casting $Cu_{47}Ti_{34}Zr_{11}Ni_8$ in a 1 × 10 × ~20 mm (thickness by width by length) copper mold. The samples were cut into pieces of cross section 10 × 10 mm and then isothermally annealed at 673, 683, 693, 708, and 723 K for 15 h and 743 K for 1 h in a vacuum furnace at a vacuum of 1×10^{-5} mbar. X-ray diffraction (XRD) was also performed on these specimens using a *Scintag Pad V X-ray Powder Diffractometer* with Cu Kα radiation on a theta - 2 theta goniometer equipped with a germanium solid state detector.

3.2. Crystallization: Results

DSC scans of as-prepared and heat-treated $Cu_{47}Ti_{34}Zr_{11}Ni_8$ are shown in Fig. 13. When heating the as-prepared amorphous solid from room temperature, three exothermic peaks are observed (upper scan in Fig. 13). To observe the thermal behavior of the alloy after heating through these exotherms, two samples were heated to 748 K and 803 K at

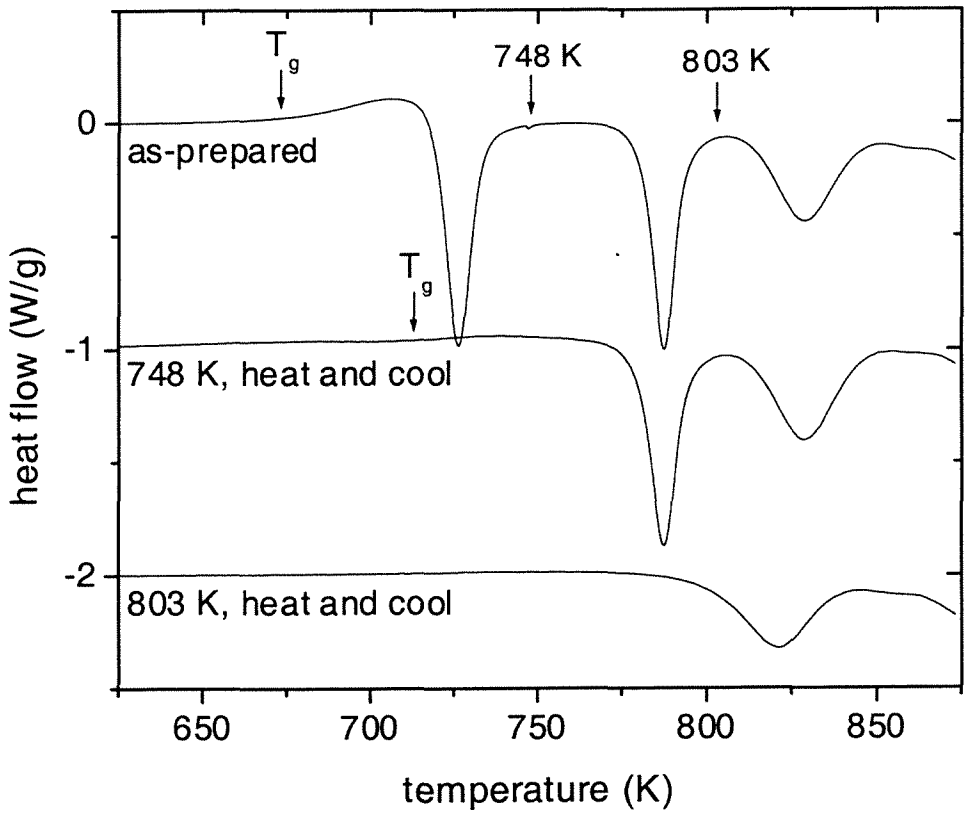

Fig. 13 DSC scans of as-prepared and heat-treated $Cu_{47}Ti_{34}Zr_{11}Ni_8$

DSC scans were performed at a heating rate of 0.333 K/s. The glass transition temperatures of the as-prepared (T_g = 673 K) and the 748 K heat-treated (T_g = 713 K) samples are indicated.

0.333 K/s and cooled to room temperature at 3.33 K/s. For both the 748 K and the 803 K heat treatments, the crystallization exotherms passed were not seen in subsequent DSC scans (lower scans in Fig. 13). The amorphous matrix of the 748 K heat-treated sample has a glass transition temperature, T_g, of 713 K, due to a shift in composition from the as-prepared state (T_g = 673 K).

A TEM dark field micrograph and electron diffraction pattern of the 748 K heat-treated sample are shown in Fig. 14, revealing 2 to 3 nm nanocrystals in an amorphous matrix. Compared to the electron diffraction pattern from an as-prepared sample, the inner diffraction ring is sharper and the outer diffraction region is split due to the formation of these nanocrystals. This sharpening of the inner diffraction ring was also observed in annealed $Zr_{41.2}Ti_{13.8}Cu_{12.5}Ni_{10}Be_{22.5}$ [57]. A TEM dark field micrograph and electron diffraction pattern of the 803 K heat-treated sample are shown in Fig. 15, revealing 5 nm and larger nanocrystals in an amorphous matrix. The phases in both samples could not be identified from the electron diffraction patterns.

To try to identify the primary nucleating phase in this alloy in the supercooled liquid temperature regime, isothermal anneals were performed at temperatures around the observed glass transition temperature of $Cu_{47}Ti_{34}Zr_{11}Ni_8$. A TEM dark field micrograph and electron diffraction pattern of a sample isothermally annealed at 701 K for 24 h are shown in Fig. 16. Nanocrystals of 5 nm in size in an amorphous matrix are observed. The nanocrystals were identified as a face centered cubic (fcc) phase with lattice parameter a = 0.38 nm. Fig. 17 includes a DSC scan of this sample; the first exotherm in the DSC scan is not present, and the remaining exotherms are broader than in the as-prepared sample (first scan in Fig. 17). The other DSC scans of isothermally annealed

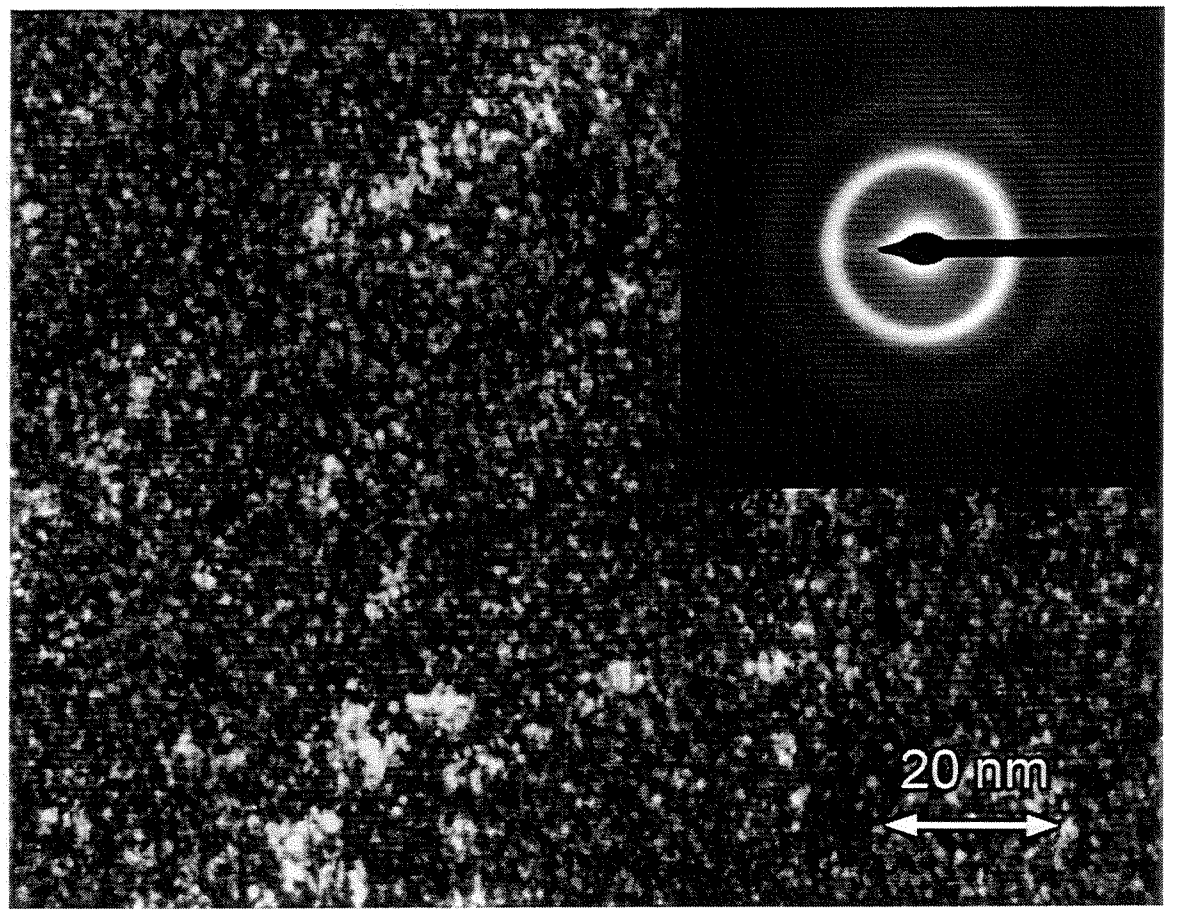

Fig. 14 Dark field TEM micrograph and electron diffraction pattern of $Cu_{47}Ti_{34}Zr_{11}Ni_8$ *heated to 748 K at 0.333 K/s and cooled at 3.33 K/s*

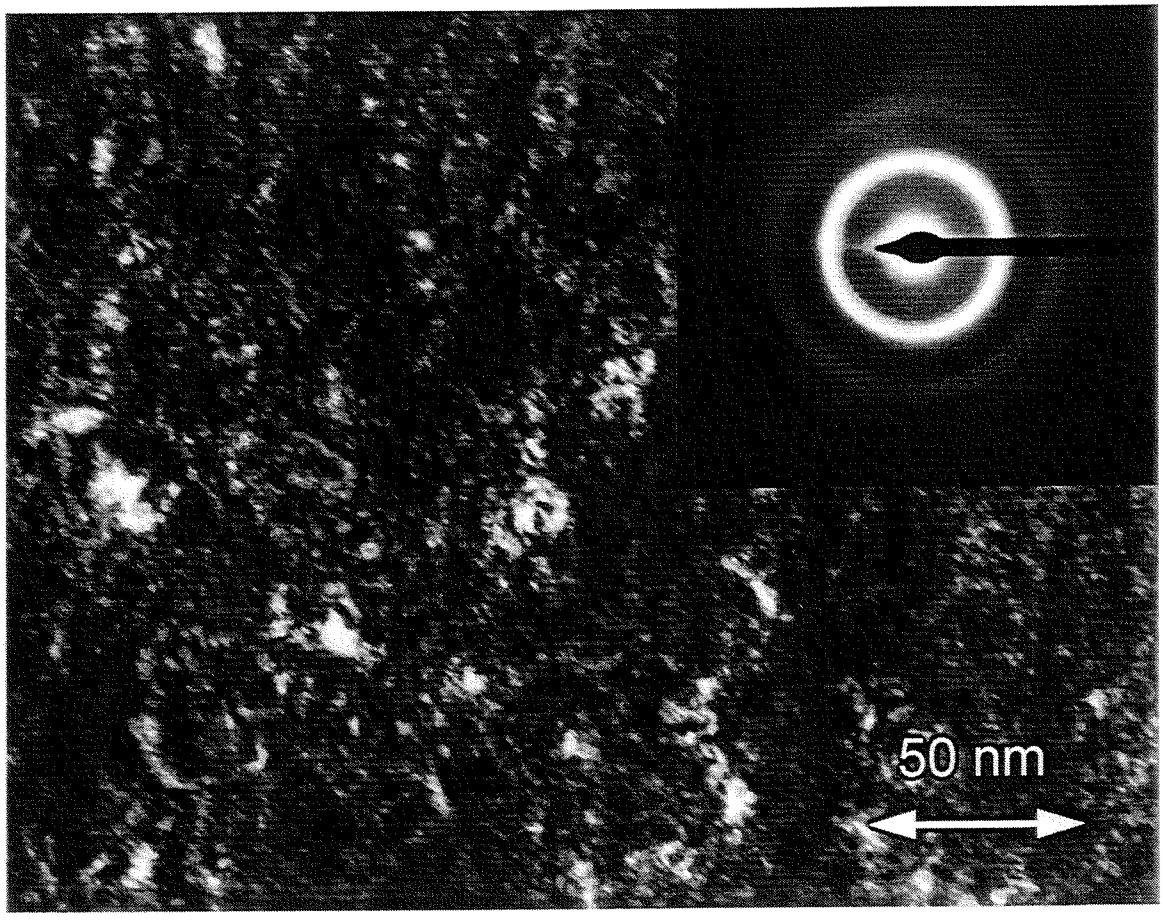

Fig. 15 Dark field TEM micrograph and electron diffraction pattern of $Cu_{47}Ti_{34}Zr_{11}Ni_8$ *heated to 803 K at 0.333 K/s and cooled at 3.33 K/s*

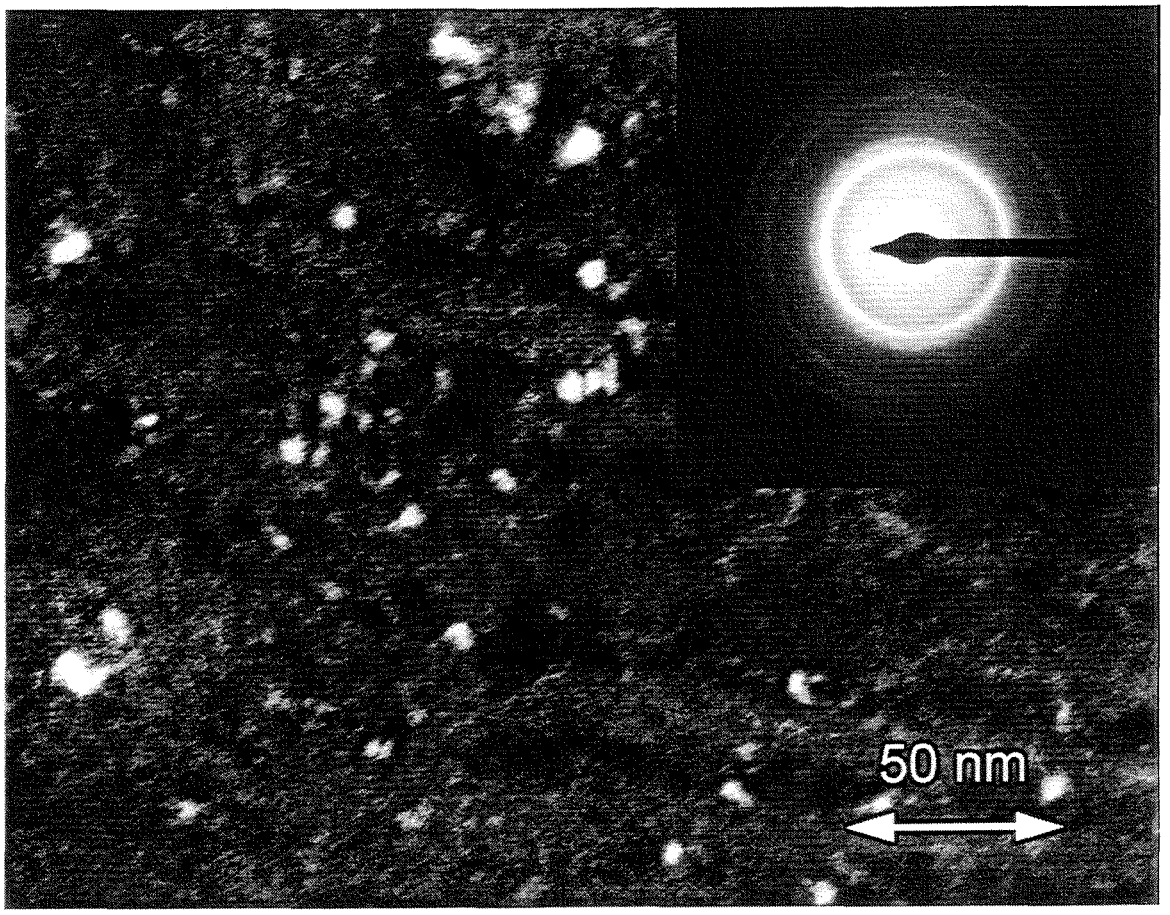

Fig. 16 Dark field TEM micrograph and electron diffraction pattern of $Cu_{47}Ti_{34}Zr_{11}Ni_8$ *isothermally annealed at 701 K for 24 hours*

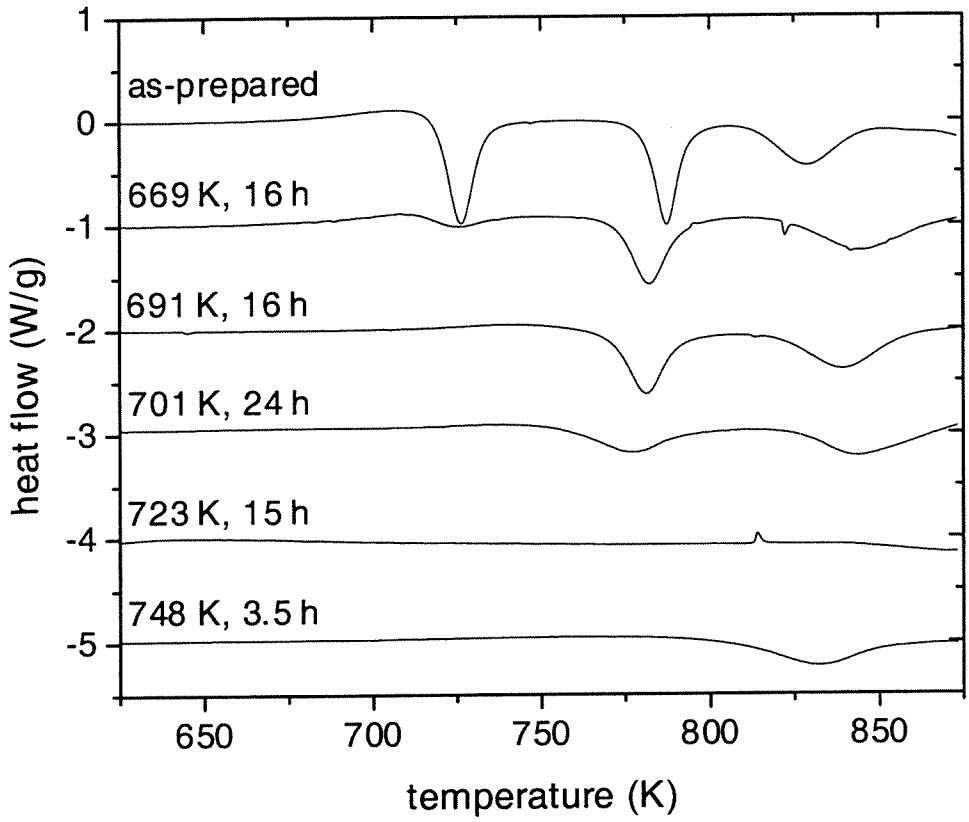

Fig. 17 DSC scans of as-prepared and isothermally annealed $Cu_{47}Ti_{34}Zr_{11}Ni_8$ *DSC scans were performed at a heating rate of 0.333 K/s. The isothermal annealing conditions are indicated in the figure.*

$Cu_{47}Ti_{34}Zr_{11}Ni_8$ shown in Fig. 17 will be discussed in conjunction with the further TEM and X-ray diffraction results.

To try to identify the phase in the 748 K heat-treated sample, a sample was isothermally annealed at 748 K for 3.5 h. A TEM dark field micrograph and electron diffraction pattern of this sample are shown in Fig. 18. Nanocrystals of an average size of 5 to 10 nm in an amorphous matrix were observed. The phases in this sample could not be identified in the electron diffraction pattern. However, similar phases are nucleating and growing in this sample and in the 803 K heat-treated sample, as evidenced by the diffraction patterns (Figs. 15 and 18). After the isothermal anneal at 748 K for 3.5 h, the first and second exothermic peaks are not present in the DSC scan (lowest scan in Fig. 17).

A sample isothermally annealed at 691 K for 16 h and observed in the TEM (micrograph not shown) revealed 1 nm and smaller nanocrystals. A DSC scan of this sample (Fig. 17) shows that the first crystallization exotherm is reduced in magnitude, while the second and third crystallization exotherms are still present.

X-ray diffraction patterns of as-prepared and isothermally annealed $Cu_{47}Ti_{34}Zr_{11}Ni_8$ are shown in Fig. 19. The samples isothermally annealed at 673, 683, and 693 K for 15 h exhibit small peaks on the broad amorphous hump, due to nanocrystals forming in the amorphous matrix. The samples isothermally annealed at 708, 723, and 803 K for 15 h and 743 K for 1 h show further evidence of crystallization, with the amorphous background diminishing and the crystalline peak becoming more intense. A DSC scan of the sample annealed at 723 K for 15 h (Fig. 17) shows no crystallization exotherms, giving evidence that the sample has a high density of

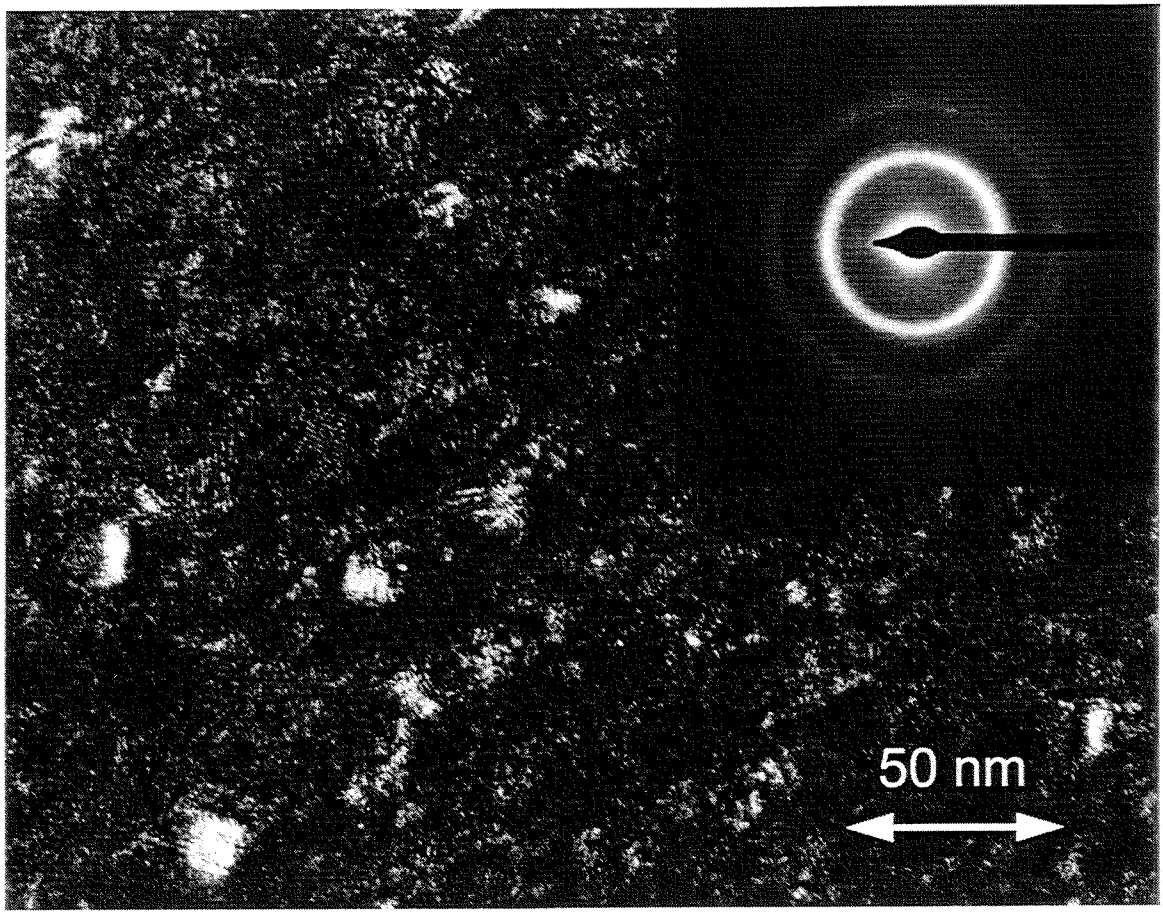

Fig. 18 Dark field TEM micrograph and electron diffraction pattern of $Cu_{47}Ti_{34}Zr_{11}Ni_8$ *isothermally annealed at 748 K for 3.5 hours*

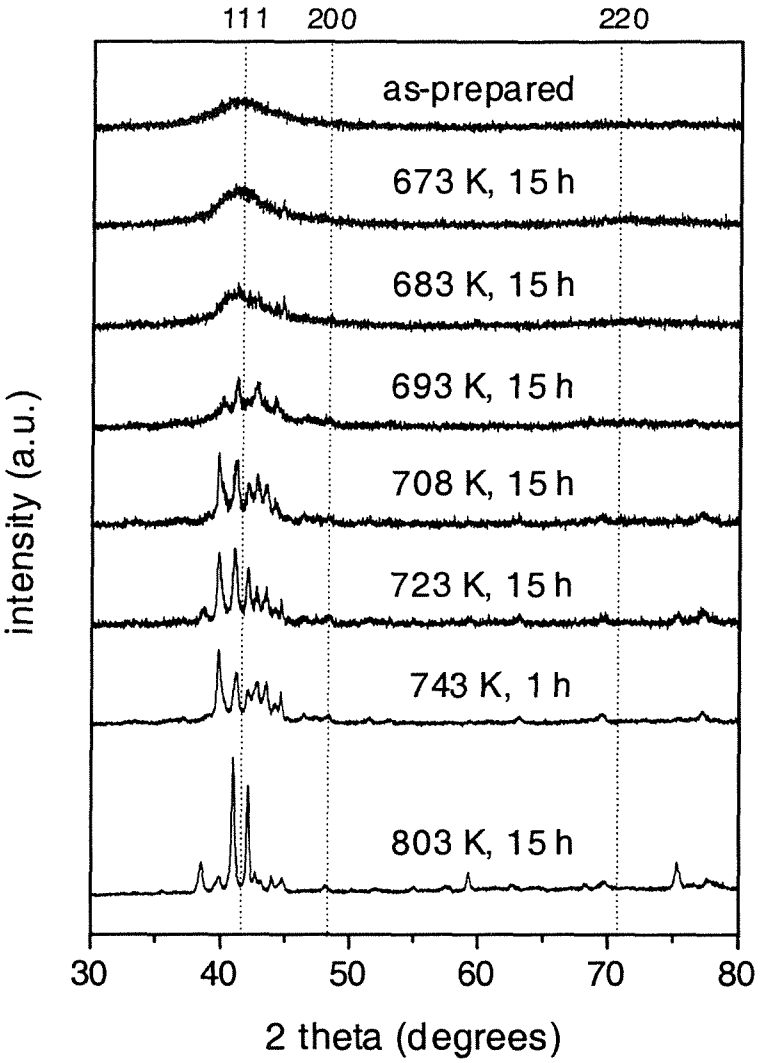

Fig. 19 X-ray diffraction patterns of as-prepared and isothermally annealed $Cu_{47}Ti_{34}Zr_{11}Ni_8$

The dotted lines on the graph represent the positions of the 111, 200, and 220 peaks of the FCC phase observed in TEM. The scans performed on the 743 K, 1 h and the 803 K, 15 h isothermally annealed samples have an improved signal to noise ratio due to longer scanning times. The isothermal annealing conditions are indicated in the figure.

nanocrystals. From the overlay of the peak positions of the primary nucleating fcc phase (TEM work), it does not appear that this fcc phase is present in the higher temperature annealed samples. More complex intermetallic phases nucleate and grow with higher temperature isothermal anneals.

Field ion micrographs of as-prepared and isothermally annealed (701 K for 24 h) $Cu_{47}Ti_{34}Zr_{11}Ni_8$ are shown in Fig. 20. Field ion microscopy of the as-prepared $Cu_{47}Ti_{34}Zr_{11}Ni_8$ showed a random distribution of spots, characteristic of an amorphous structure. Also, no ring patterns (poles), which result from a crystalline structure, were observed. The isothermally annealed $Cu_{47}Ti_{34}Zr_{11}Ni_8$ revealed nanocrystals in an amorphous matrix, as also evidenced by TEM. The composition of one nanocrystal was measured as 79.31 ± 1.06 at. % Ti, 19.20 ± 1.03% Zr, 0.14 ± 0.10% Cu, and 0.34 ± 0.15% Ni.

For analysis of atom probe tomography data, the three-dimensional map of atoms collected from a cylinder of material in the specimen is divided into small blocks of atoms (100 atoms per block) and a frequency distribution of the composition of each atomic species in each individual block is constructed. These frequency distributions are compared to the frequency distribution expected from a random distribution of atoms in an alloy of the same mean composition to determine whether phase separation has occurred. Frequency distributions generated by different models of decomposition are then generated and fit to the experimentally measured frequency distribution; parameters contained in these models are then compared, giving a measure of the composition differences in decomposed regions.

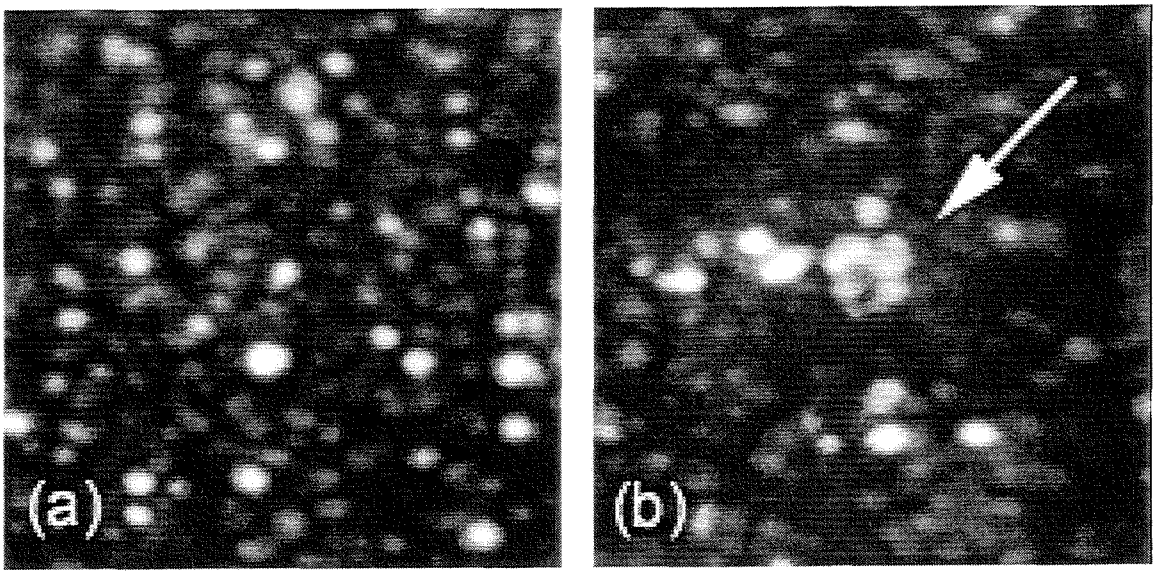

Fig. 20 Field ion micrographs of (a) as-prepared and (b) isothermally annealed (701 K for 24 h) $Cu_{47}Ti_{34}Zr_{11}Ni_8$

The spots in the micrographs represent atoms in the sample. The arrow in (b) highlights a nanocrystal. A scale was not included due to inaccuracies in determining the length scale in the micrographs.

The two models used to generate probability distributions for a phase separated sample in this investigation were the sinusoidal or P_a model [58] and the Langer, Bar-on, and Miller (LBM) model [59]. The P_a model considers decomposition to occur spinodally and is based on a sinusoidal variation in composition. The P_a model considers different samples from a discretized composition profile

$$p_j = P_0 + P_a \sin\left[\frac{2\pi j}{n_d}\right], \quad \{j : 0 \le j \le n_d\}, \tag{27}$$

where $2P_a$ is the peak-to-peak amplitude of the spinodal, P_0 is the mean composition, and n_d is the discretization, i.e., a number chosen to ensure that the estimate is independent of n_d ($n_d = 20$, in these calculations). The maximum likelihood estimates of composition amplitudes are then calculated. The P_a model has one independent parameter, P_a. The difference in the composition of the two decomposed phases is given by $\Delta c = 2P_a$. The results of the statistical analysis with the P_a model are listed in Table III for the data sets collected (one as-prepared sample and two isothermally annealed samples). The standard error is the error in the P_a value. The χ^2 and the degrees of freedom values are used to determine the confidence level of the fit.

$Cu_{47}Ti_{34}Zr_{11}Ni_8$ exhibits phase separation primarily through the partitioning of copper and titanium in both the as-prepared and isothermally annealed states, as evidenced by the Δc values. In one of the isothermally annealed specimens, the degree of decomposition is more than in the as-prepared state. In the other isothermally annealed specimen, the degree of decomposition is of the same magnitude as in the as-prepared sample. This difference is probably due to regional variations and possibly due to the

as-prepared $Cu_{47}Ti_{34}Zr_{11}Ni_8$

	P_a	Standard error	χ^2	Degrees of freedom	$\Delta c = 2P_a$
Cu	0.068	0.008	18.0	24	0.136
Ti	0.056	0.008	20.2	23	0.112
Zr	0.000		3.9	13	0.000
Ni	0.007	0.006	8.4	10	0.014

isothermally annealed (701 K for 24 h) $Cu_{47}Ti_{34}Zr_{11}Ni_8$

	P_a	Standard error	χ^2	Degrees of freedom	$\Delta c = 2P_a$
Cu	0.108	0.004	**217.6**	39	0.216
Ti	0.108	0.005	**345.1**	40	0.216
Zr	0.028	0.002	15.9	19	0.056
Ni	0.019	0.001	9.8	14	0.058

isothermally annealed (701 K for 24 h) $Cu_{47}Ti_{34}Zr_{11}Ni_8$

	P_a	Standard error	χ^2	Degrees of freedom	$\Delta c = 2P_a$
Cu	0.073	0.007	21.0	26	0.146
Ti	0.056	0.007	20.3	24	0.112
Zr	0.021	0.004	6.7	15	0.042
Ni	0.032	0.002	**29.2**	15	0.064

The parameters P_a and Δc are given in atomic fraction. Bold entries in the χ^2 column indicate the fit is rejected at the 95% level.

Table III The results of the statistical analysis using the P_a model for $Cu_{47}Ti_{34}Zr_{11}Ni_8$

FIM/APT samples being taken from different areas of the 1 mm thick strip of the bulk material. Further analysis of the data with contingency tables showed that the copper and titanium are antisegregated; i.e., the copper-enriched regions are low in titanium and vice versa.

The LBM model considers non-linear spinodal decomposition using a double Gaussian distribution with the probability distribution function

$$P(c)=\frac{\mu_2 \exp\left[\frac{-(c-\mu_1)^2}{2\sigma^2}\right]+\mu_1 \exp\left[\frac{-(c-\mu_2)^2}{2\sigma^2}\right]}{(\mu_1+\mu_2)\sigma\sqrt{2\pi}}. \qquad (28)$$

One Gaussian is centered at μ_1, the other is center at μ_2, and both have a width σ. The LBM model has three independent parameters, μ_1, μ_2, and σ. In implementations of the LBM model, the two parameters $b_1 = c_0 - \mu_1$ and $b_2 = \mu_2 - c_0$, where c_0 is the mean concentration, are substituted into the equation. The difference in the composition of two decomposed phases is given by $\Delta c = b_1 + b_2$. The results of the statistical analysis with the LBM model are listed in Table IV for the data sets collected. As in the P_a model, the Δc values in the LBM model show that the alloy primarily decomposes to copper-enriched and titanium-enriched regions. Further details on both the P_a and the LBM models can be found in Refs. 60 and 61.

Data from the SANS experiments, scattering cross section $S(Q)$ versus scattering vector Q, are shown in Fig. 21. The as-prepared and the isothermally annealed at 673 K for 15 h samples exhibit no scattering signal, i.e., these samples have no detectable composition fluctuations in a size regime from 1 to 150 nm. The samples isothermally annealed at higher temperatures all exhibit interference peaks, giving evidence of

as-prepared $Cu_{47}Ti_{34}Zr_{11}Ni_8$

	b_1	b_2	σ	χ^2	Degrees of freedom	$\Delta c = b_1 + b_2$
Cu	0.040	0.050	0.020	16.870	24	0.090
Ti	0.050	0.030	0.010	19.313	23	0.080
Zr	0.010	0.010	0.010	8.842	14	0.020
Ni	0.010	0.010	0.010	11.997	11	0.020

isothermally annealed (701 K for 24 h) $Cu_{47}Ti_{34}Zr_{11}Ni_8$

	b_1	b_2	σ	χ^2	Degrees of freedom	$\Delta c = b_1 + b_2$
Cu	0.100	0.030	0.060	39.114	42	0.130
Ti	0.010	0.160	0.070	43.979	45	0.170
Zr	0.010	0.030	0.010	19.531	20	0.050
Ni	0.010	0.010	0.010	8.782	14	0.020

isothermally annealed (701 K for 24 h) $Cu_{47}Ti_{34}Zr_{11}Ni_8$

	b_1	b_2	σ	χ^2	Degrees of freedom	$\Delta c = b_1 + b_2$
Cu	0.020	0.070	0.040	17.918	27	0.090
Ti	0.050	0.030	0.010	18.842	24	0.080
Zr	0.010	0.020	0.010	6.254	15	0.030
Ni	0.070	0.010	0.010	10.407	15	0.080

The parameters b_1, b_2, σ, and Δc are given in atomic fraction.

Table IV The results of the statistical analysis using the LBM model for $Cu_{47}Ti_{34}Zr_{11}Ni_8$

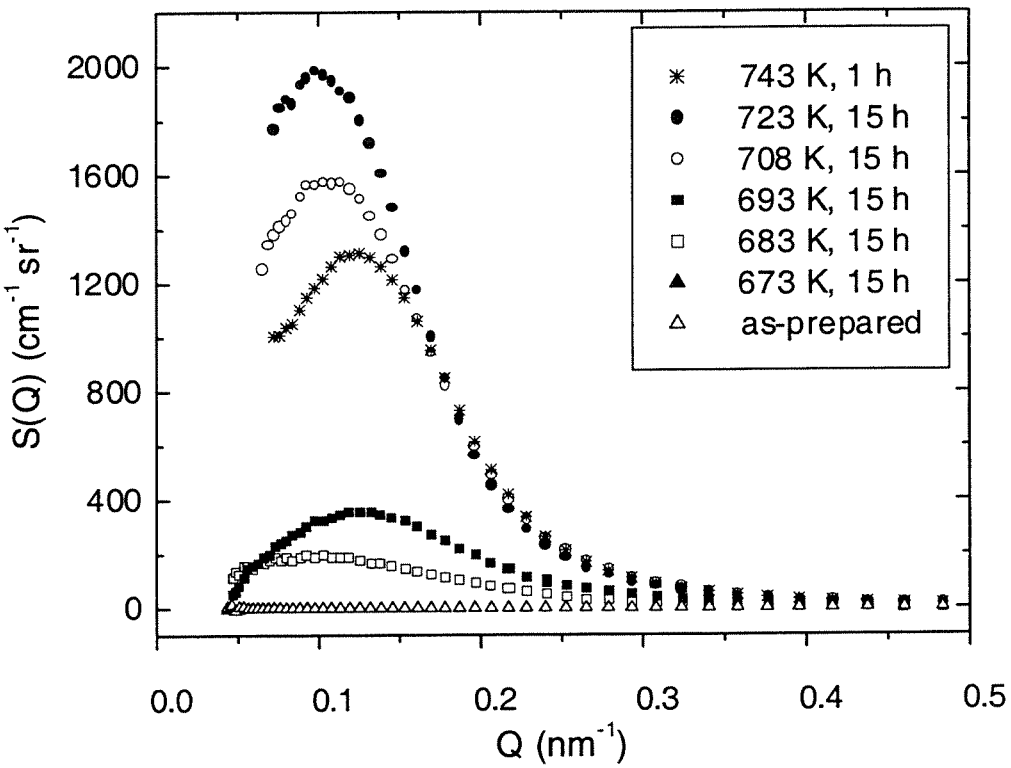

Fig. 21 SANS data from as-prepared and isothermally annealed $Cu_{47}Ti_{34}Zr_{11}Ni_8$

Isothermal annealing conditions are indicated in the legend. The data from the as-prepared and the 673 K, 15 h isothermally annealed samples lie on top of each other.

scattering inhomogeneities. In these higher temperature annealed samples, the inhomogeneities are nanocrystals in the amorphous matrix, as shown by TEM. The intensity of the interference peaks increase with increasing temperature, due to the increase in the volume fraction of the scattering nanocrystals.

After a sample was held for a period of time at an elevated temperature during isothermal DSC experiments, a broad exothermic heat release, on the order of 1 kJ g-atom^{-1}, was observed. This heat release is due to the formation of nanocrystals. An Arrhenius plot, with the points indicating the onset of the heat release, is shown in Fig. 22. The onset of the heat release follows an Arrhenius law,

$$\frac{1}{t} \propto \exp\left(\frac{-E}{k_B T}\right), \tag{29}$$

where t is time (in seconds). The activation energy is $E = 4.28\ (\pm 0.11)$ eV, obtained by a fit to the data.

3.3. Crystallization: Discussion

$Zr_{41.2}Ti_{13.8}Cu_{12.5}Ni_{10}Be_{22.5}$, with a critical cooling rate of 1 K/s for glass formation [62], is one of the best metallic glass-forming alloys yet developed. The thermophysical properties of $Zr_{41.2}Ti_{13.8}Cu_{12.5}Ni_{10}Be_{22.5}$ have been well characterized, including its crystallization behavior. Crystallization at lower temperatures (achieved by isothermally annealing samples near the glass transition temperature) proceeds by the alloy decomposing to titanium-enriched regions [48, 49], followed by the polymorphic nucleation of metastable face centered cubic Cu-Ti nanocrystals (a = 0.40 nm) in these titanium-enriched regions. In situ SANS experiments support the idea that a chemical

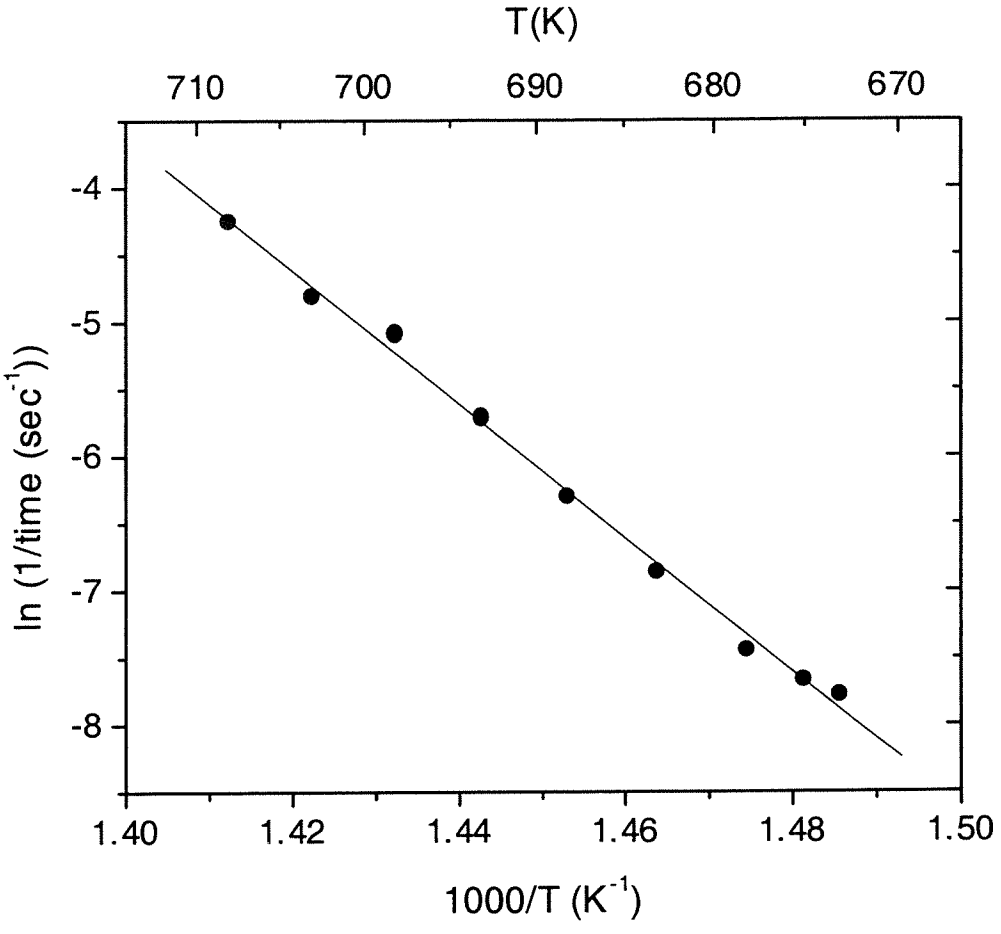

Fig. 22 Arrhenius plot of data obtained from isothermal anneals of $Cu_{47}Ti_{34}Zr_{11}Ni_8$

Points indicate the time when heat (~1 kJ g-atom^{-1}*) was released from the sample during the isothermal anneal.*

decomposition on a nanometer scale involving titanium initiates an abrupt onset of nucleation, resulting in a microstructure of nanocrystals in an amorphous matrix [55].

The crystallization of the $Cu_{47}Ti_{34}Zr_{11}Ni_8$ glass-forming alloy shows similarities to that of $Zr_{41.2}Ti_{13.8}Cu_{12.5}Ni_{10}Be_{22.5}$. Decomposition into copper-enriched and titanium-enriched regions was observed in the as-prepared and isothermally annealed states; regions high in copper content are low in titanium content and vice versa. Face centered cubic nanocrystals, with a lattice parameter of a = 0.38 nm, nucleated and grew in the amorphous matrix. The composition of one nanocrystal was determined by atom probe tomography in the sample isothermally annealed at 701 K for 24 h. This nanocrystal contained about 80% titanium and 20% zirconium, and thus presumably nucleated in a titanium-enriched phase separated region. However, this result does not exclude nanocrystals of other compositions forming.

According to the titanium-zirconium phase diagram [11], titanium and zirconium form a hexagonal close packed solid solution at all compositions. Face centered cubic titanium and zirconium phases can be formed at high pressures at 700 K (the temperature of the heat treatment for the TEM and APT experiments), but the free energy of formation of these face centered cubic phases is ~250 kJ/mol [63]. Therefore, it is unlikely that the titanium-zirconium nanocrystal detected in the FIM/APT corresponds to the face centered cubic phase detected in the TEM.

Simple arguments [14] show that the cooling rate for a metallic glass-forming alloy during processing is related to the casting thickness by

$$\frac{dT}{dt}\left[\frac{K}{s}\right] = \frac{10}{(R[cm]/2)^2}, \qquad (30)$$

where R (cm) is the specimen thickness. The microstructure of the beams analyzed in the atom probe represent the state of the alloy when it is cooled from the melt at ~4000 K/s by casting the alloy in 1 mm thick strips. From the P_a and LBM models, decomposition is already present in a sample cooled at this rate. Isothermally annealing the alloy increased the magnitude of decomposition, as seen in the Δc values.

Previous work by Miller et al. [64] on as-prepared $Cu_{47}Ti_{34}Zr_{11}Ni_8$ revealed solute clustering, with antisegregation of copper and titanium, as well as nanocrystals in the amorphous matrix. No nanocrystals were observed in the as-prepared $Cu_{47}Ti_{34}Zr_{11}Ni_8$ samples in this study. The samples Miller et al. used were prepared with a lower cooling rate of ~1000 K/s (by casting the alloy in 2 mm thick strips), which presumably allowed enough time for the nucleation of nanocrystals.

The fact that $Cu_{47}Ti_{34}Zr_{11}Ni_8$ phase separates followed by nanocrystals forming is also supported by the SANS measurements, which show an interference maximum for the isothermally annealed samples. The SANS intensity, however, is one to two orders of magnitude higher than that in similar experiments performed on annealed $Zr_{41.2}Ti_{13.8}Cu_{12.5}Ni_{10}Be_{22.5}$ [53, 55] and $Zr_{52.5}Cu_{17.9}Ni_{14.6}Al_{10}Ti_5$ [51]. This is due to the larger amount of titanium, which has a negative scattering length, present in $Cu_{47}Ti_{34}Zr_{11}Ni_8$. The scattering intensity of the samples annealed for 15 h at 708 and 723 K is larger than that of the sample annealed for 1 h at 743 K. Thus, nanocrystallization is not complete after 1 h of annealing, even at a temperature of 70 K above T_g. This is in agreement with the DSC scans in Fig. 17, where an exothermic peak is still visible after 3.5 h annealing at 748 K, but no peak is observed after 15 h annealing at 723 K. One

possibility is that the nucleation rate at similar temperatures above T_g (i.e., T - T_g) is much lower in $Cu_{47}Ti_{34}Zr_{11}Ni_8$ than in $Zr_{41.2}Ti_{13.8}Cu_{12.5}Ni_{10}Be_{22.5}$ and $Zr_{52.5}Cu_{17.9}Ni_{14.6}Al_{10}Ti_5$.

Furthermore, in contrast to observations on $Zr_{41.2}Ti_{13.8}Cu_{12.5}Ni_{10}Be_{22.5}$ and $Zr_{52.5}Cu_{17.9}Ni_{14.6}Al_{10}Ti_5$, the Q values of the interference peaks, Q_{max}, do not systematically shift to lower values with increasing annealing temperature in $Cu_{47}Ti_{34}Zr_{11}Ni_8$, as is expected with a mechanism of spinodal decomposition [65]. The interference maximum, Q_{max}, is approximately 0.1 nm^{-1} in $Cu_{47}Ti_{34}Zr_{11}Ni_8$; Q_{max} shifts from 0.4 to 0.1 nm^{-1} in $Zr_{41.2}Ti_{13.8}Cu_{12.5}Ni_{10}Be_{22.5}$, and from 0.3 to 0.2 nm^{-1} in $Zr_{52.5}Cu_{17.9}Ni_{14.6}Al_{10}Ti_5$, for similar annealing temperatures above T_g. Although TEM shows similar results for $Zr_{41.2}Ti_{13.8}Cu_{12.5}Ni_{10}Be_{22.5}$ and $Cu_{47}Ti_{34}Zr_{11}Ni_8$, the crystallization process of $Cu_{47}Ti_{34}Zr_{11}Ni_8$ may differ from that in zirconium based alloys. Additional in situ small-angle X-ray scattering experiments have been performed on $Cu_{47}Ti_{34}Zr_{11}Ni_8$ to further investigate the crystallization process [66].

The onset of nucleation data from the isothermal DSC experiments follows an Arrhenius law. The activation energy calculated, E = 4.28 (± 0.11) eV, is comparable to the value attributed to titanium diffusion in $Zr_{41.2}Ti_{13.8}Cu_{12.5}Ni_{10}Be_{22.5}$ (E = 4.09 (± 0.76) eV) [55, 67]. This suggests that the nucleation of nanocrystals in $Cu_{47}Ti_{34}Zr_{11}Ni_8$ is a diffusion-controlled process.

In summary, different experimental techniques were used to investigate the crystallization of amorphous $Cu_{47}Ti_{34}Zr_{11}Ni_8$. Similar to other metallic glass-forming alloys, $Cu_{47}Ti_{34}Zr_{11}Ni_8$ phase separates prior to crystallization. $Cu_{47}Ti_{34}Zr_{11}Ni_8$ decomposes to copper-enriched and titanium-enriched regions (the copper-enriched regions are low in titanium content and vice versa). The primary nucleating phase has a

face centered cubic structure. More complex intermetallic phases nucleate and grow in the alloy with higher temperature isothermal anneals.

4. THE EFFECT OF SMALL ALLOYING ADDITIONS ON THE THERMAL STABILITY OF $Cu_{47}Ti_{34}Zr_{11}Ni_8$

Progressively higher order alloy systems (binary, ternary, quarternary, and quintary alloys) exhibit progressively better glass-forming ability for compositions optimized for glass formation [47]. This can be viewed in terms of the 'confusion principle' [9], the idea that crystallization in a complex alloy made up of many different elements (especially elements of different atomic sizes) is frustrated compared to an alloy with fewer elements.

Small additions of another element to a metallic glass-forming alloy can dramatically improve the thermal stability of the alloy. In the case of boron additions to a Pd-Cu-Si alloy [68], the thermal stability of the supercooled liquid against crystallization is improved, which was attributed to an increase in the dense random packing of the supercooled liquid, making atomic diffusion more difficult. Boron additions were also made to the Zr-Cu-Al alloy [69], again improving the thermal stability of the supercooled liquid against crystallization, which was attributed to the boron destabilizing the primary nucleating phases.

Silicon has also been found to influence the thermal stability and glass-forming ability of metallic glass-forming alloys. This effect is likely due to the silicon addition destabilizing catalytic heterogeneous nucleation sites formed by oxygen in the alloys. Oxygen impurities in titanium-zirconium based metallic glass-forming alloys reduce the glass-forming ability of the alloy, which Lin et al. [70] demonstrated in work performed on $Zr_{52.5}Cu_{17.9}Ni_{14.6}Al_{10}Ti_5$, where oxygen was intentionally incorporated into the alloy.

In work performed on Ni-Pd-P alloys, Volkert [71] found that 1% atomic additions of silicon to the alloy increased the glass-forming ability of the alloy; this was attributed to silicon destabilizing P_2O_5 clusters that possibly acted as heterogeneous nucleation sites. In work performed on $Cu_{47}Ti_{34}Zr_{11}Ni_8$ reinforced with SiC particles, Choi-Yim et al. [72] found that small additions of silicon to this alloy improve both the stability of the supercooled liquid against crystallization and the glass-forming ability of the alloy. 1% silicon additions, substituted for titanium, yielded the best results. They also found that the reduced glass transition temperatures, the heat capacity differences at the glass transition, and the entropies of fusion for $Cu_{47}Ti_{34}Zr_{11}Ni_8$ and $Cu_{47}Ti_{33}Zr_{11}Ni_8Si_1$ coincide, so the thermodynamics of $Cu_{47}Ti_{34}Zr_{11}Ni_8$ are not altered by the addition of silicon. Furthermore, the activation energy for crystallization and the relaxation kinetics are not significantly different in the two alloys, indicating that the growth kinetics and the structural relaxation times for these alloys are similar. Since the thermodynamics and the kinetics of the alloy were not significantly altered with small additions of silicon, Choi-Yim et al. suggested that silicon destabilizes oxide nucleating sites via Si-O interactions.

To further study the role of silicon in the improvements in the thermal stability of $Cu_{47}Ti_{34}Zr_{11}Ni_8$, an investigation of as-prepared and isothermally annealed $Cu_{47}Ti_{34}Zr_{11}Ni_8$ and $Cu_{47}Ti_{33}Zr_{11}Ni_8Si_1$ using transmission electron microscopy (TEM), field ion microscopy (FIM), and atom probe tomography (APT) was performed. TEM can identify small crystalline regions in these samples. APT has a high spatial resolution, which can determine the local composition shifts, if any, around a silicon atom. These results are presented in chapter 4.1. Experiments were also performed to determine the

effect of small additions of magnesium and germanium on the thermal stability of $Cu_{47}Ti_{34}Zr_{11}Ni_8$, the results of which are presented in chapter 4.2.

4.1. TEM and FIM/APT Investigation of $Cu_{47}Ti_{33}Zr_{11}Ni_8Si_1$

Alloys of nominal compositions $Cu_{47}Ti_{34}Zr_{11}Ni_8$ and $Cu_{47}Ti_{33}Zr_{11}Ni_8Si_1$ were prepared in an arc melter with a titanium gettered, ultrahigh purity argon atmosphere, with elements of purities from 99.9% to 99.9999%. The silicon containing alloy was prepared by first melting the silicon with the copper to avoid forming any high melting point silicides; the other elements were alloyed with each other as well. Then, the two ingots were alloyed to obtain the desired composition. All ingots were melted repeatedly to promote homogeneity. To obtain amorphous samples, the alloys were remelted in fused quartz tubes in a high frequency induction furnace and then injection cast with ultrahigh purity argon into a copper mold.

Transmission electron microscopy (TEM) was performed with a *Phillips EM430* operating at 300 kV with a lanthanum hexaboride (LaB_6) electron source. Four samples were characterized in the TEM: as-prepared $Cu_{47}Ti_{34}Zr_{11}Ni_8$, isothermally annealed (701 K for 24 h) $Cu_{47}Ti_{34}Zr_{11}Ni_8$, as-prepared $Cu_{47}Ti_{33}Zr_{11}Ni_8Si_1$, and isothermally annealed (718 K for 24 h) $Cu_{47}Ti_{33}Zr_{11}Ni_8Si_1$. All samples were prepared by ultramicrotomy. The $Cu_{47}Ti_{33}Zr_{11}Ni_8Si_1$ sample was annealed at a higher temperature because of the higher glass transition temperature of this alloy (see Fig. 23). Isothermal anneals were performed by sealing a sample wrapped in tantalum foil in a quartz tube evacuated to a vacuum of 5×10^{-6} mbar or lower and placing this sample in an electric furnace.

Field ion microscopy (FIM) and atom probe tomography (APT) specimens were prepared by casting the alloys into a copper mold of dimensions 1 × 4 × ~25 mm (thickness by width by length). Bars of cross section ~0.15 to 0.30 mm square were cut with a diamond saw. The bars were electropolished using 12.5% sulfuric acid in methanol (~9-14 V). Some bars were subsequently electropolished with a solution of 2% perchloric acid in 2-butoxyethanol (~9 V). Four samples were characterized with FIM/APT: as-prepared $Cu_{47}Ti_{34}Zr_{11}Ni_8$, isothermally annealed (701 K for 24 h) $Cu_{47}Ti_{34}Zr_{11}Ni_8$, as-prepared $Cu_{47}Ti_{33}Zr_{11}Ni_8Si_1$, and isothermally annealed (708 K for 24 h) $Cu_{47}Ti_{33}Zr_{11}Ni_8Si_1$. The FIM/APT experiments were performed with an Energy-Compensated Optical Position-Sensitive Atom Probe (ECOPoSAP) at Oak Ridge National Laboratory. Neon was used as the imaging gas for the field ion microscopy, with a sample temperature of 60 K. For the atom probe tomography, the pulse fraction was 20% of the standing voltage and the pulse repetition rate was 1500 Hz.

DSC scans (heating rate of 0.333 K/s) of $Cu_{47}Ti_{34}Zr_{11}Ni_8$ and $Cu_{47}Ti_{33}Zr_{11}Ni_8Si_1$ are shown in Fig. 23. Differential scanning calorimetry was performed with a *Perkin Elmer DSC-7*. A measure of the thermal stability against crystallization is ΔT, the temperature interval between the onset of glass transition and crystallization. $Cu_{47}Ti_{33}Zr_{11}Ni_8Si_1$ has a significantly larger ΔT (~10 K) compared to $Cu_{47}Ti_{34}Zr_{11}Ni_8$.

Dark field micrographs and electron diffraction patterns of isothermally annealed $Cu_{47}Ti_{34}Zr_{11}Ni_8$ and $Cu_{47}Ti_{33}Zr_{11}Ni_8Si_1$ are shown in Figs. 16 and 24, respectively. Micrographs from TEM of the as-prepared $Cu_{47}Ti_{34}Zr_{11}Ni_8$ and $Cu_{47}Ti_{33}Zr_{11}Ni_8Si_1$ revealed a fine granular structure, characteristic of an amorphous structure. After the isothermal anneals, both alloys are partially crystallized, with nanocrystals embedded in

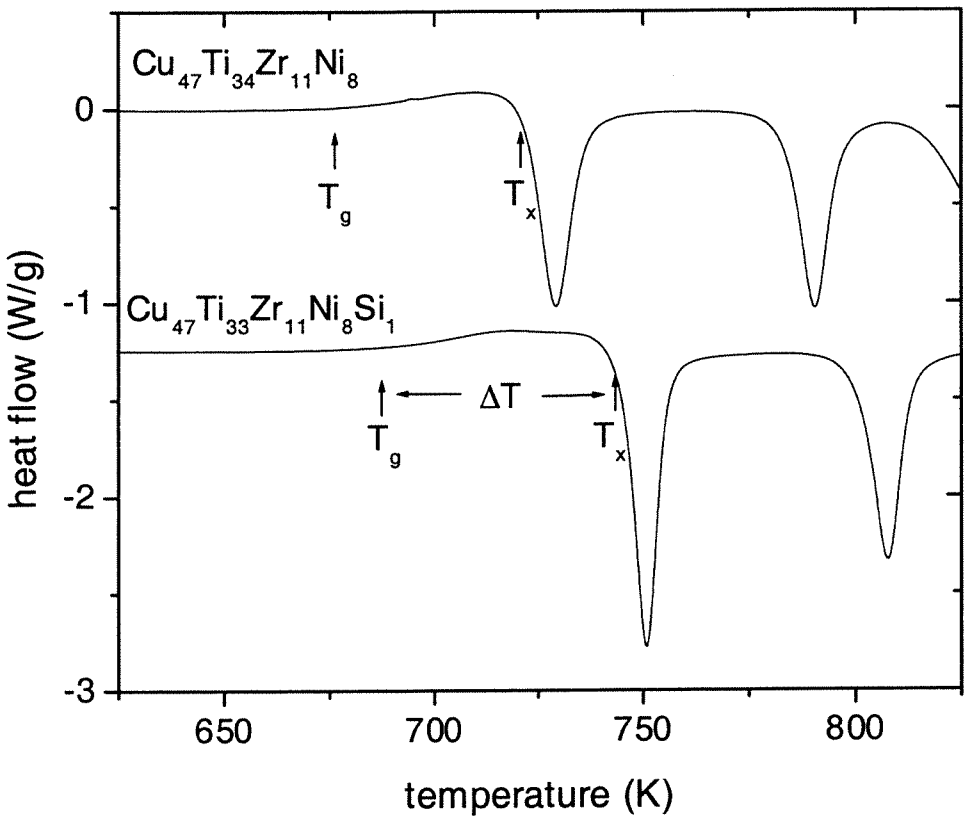

Fig. 23 DSC scans of $Cu_{47}Ti_{34}Zr_{11}Ni_8$ and $Cu_{47}Ti_{33}Zr_{11}Ni_8Si_1$

DSC scans were performed at a heating rate of 0.333 K/s. Arrows indicate the onset of the glass transition, T_g, and crystallization, T_x.

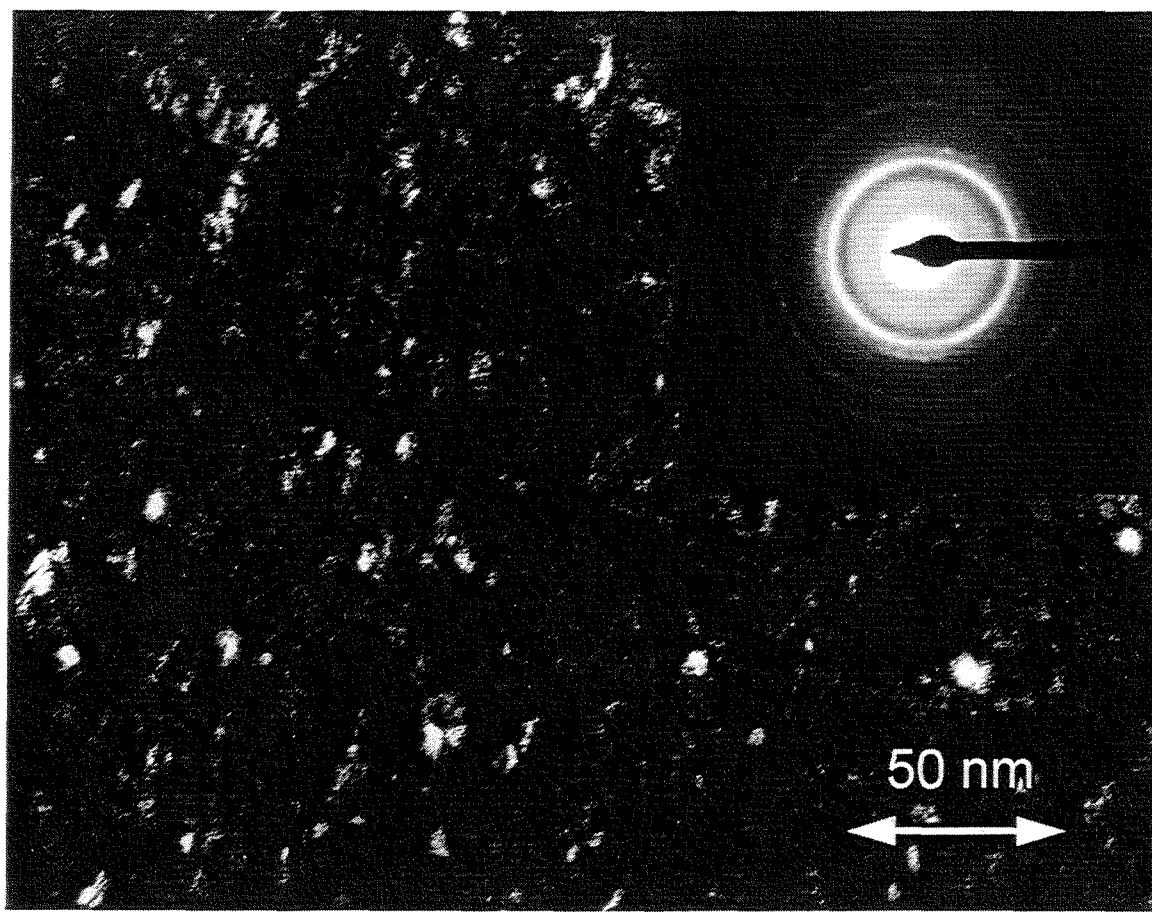

Fig. 24 Dark field TEM micrograph and electron diffraction pattern $Cu_{47}Ti_{33}Zr_{11}Ni_8Si_1$ *isothermally annealed at 718 K for 24 hours*

an amorphous matrix. The nanocrystals have a face centered cubic (fcc) structure, with the $Cu_{47}Ti_{34}Zr_{11}Ni_8$ nanocrystals (~5 nm in size) having a lattice constant of a = 0.38 nm and the $Cu_{47}Ti_{33}Zr_{11}Ni_8Si_1$ nanocrystals (~4 nm in size) having a lattice constant of a = 0.37 nm. These lattice constants are within the 5% error that is expected for lattice constant determinations with a TEM.

Field ion microscopy of the as-prepared $Cu_{47}Ti_{34}Zr_{11}Ni_8$ and $Cu_{47}Ti_{33}Zr_{11}Ni_8Si_1$ samples showed a random distribution of spots, characteristic of an amorphous structure. Also, no ring patterns (poles), which result from a crystalline structure, were observed. The isothermally annealed $Cu_{47}Ti_{34}Zr_{11}Ni_8$ and $Cu_{47}Ti_{33}Zr_{11}Ni_8Si_1$ samples showed nanocrystals in an amorphous matrix, as also evidenced by TEM.

To look at the local structure around a silicon atom in the $Cu_{47}Ti_{33}Zr_{11}Ni_8Si_1$ samples, a computer program was written to determine the nearest neighbor of each silicon atom as measured by atom probe tomography. The nearest neighbors of silicon atoms did not show any significant systematic deviation from the bulk composition of the alloy in either the as-prepared or isothermally annealed states. The computer program also calculated the composition of the alloy in spherical shells around each silicon atom. An example of these data for one as-prepared $Cu_{47}Ti_{33}Zr_{11}Ni_8Si_1$ sample are shown in Fig. 25. Again, no significant systematic deviations from the bulk composition were seen in either the as-prepared or the isothermally annealed states. The bulk composition in these samples, as determined with APT, was always ~45 at. % Ti and ~30 % Cu. APT experiments performed at lower temperatures (50 K) yielded similar results, so this difference in composition from the nominal composition is unlikely to be due to the preferential evaporation of copper.

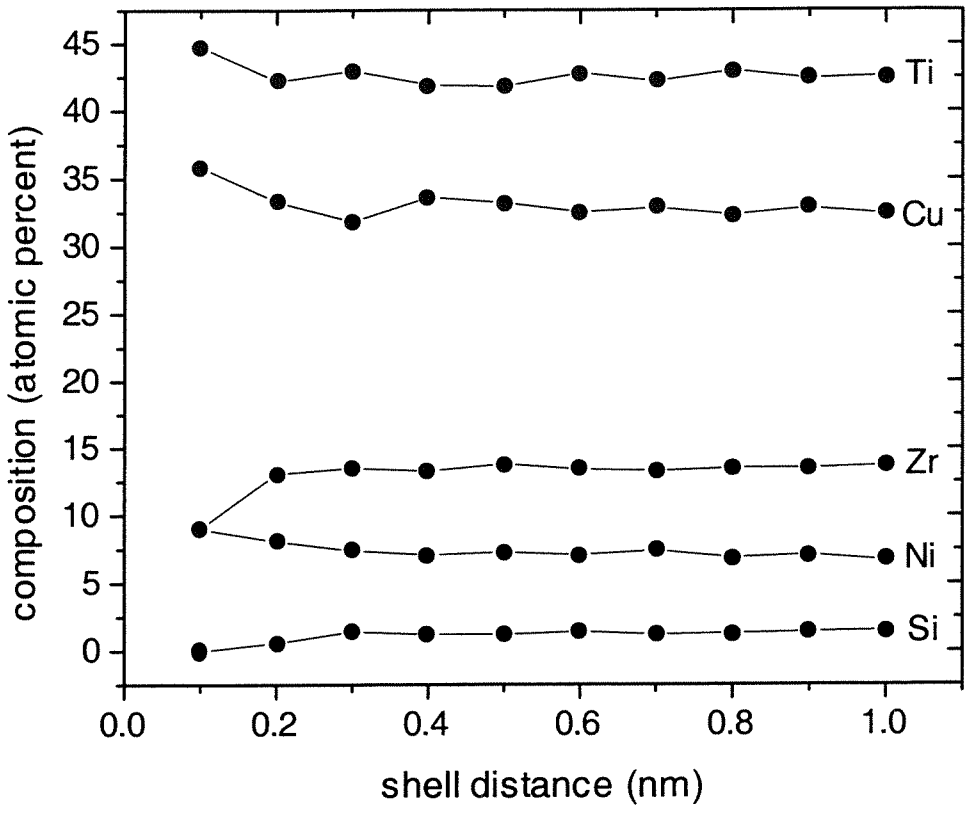

Fig. 25 Composition of the atoms surrounding each silicon atom in a sample of as-prepared $Cu_{47}Ti_{33}Zr_{11}Ni_8Si_1$

These data are from an analysis of one atom probe tomography experiment. Each spherical shell around a silicon atom is 0.1 nm thick, with the shell distance giving the outermost bound of each shell. For example, the 0.1 nm shell is the shell from 0 nm to 0.1 nm. The distances are the projected positions (a combination of the actual position plus a trajectory aberration) of atoms in the sample as measured with APT. Consequently, the interatomic spacing measured may be smaller than the interatomic spacing in the sample.

It should also be noted that the isotopes $^{16}O^{+}$ and $^{48}Ti^{3+}$ overlap in the mass-to-charge ratio spectrum. If silicon bonds with oxygen impurities in the alloy, it would be detected with APT as a high concentration of titanium around each silicon atom, which is not observed. No composition shift from the bulk composition around a silicon atom was detected within the resolution limit of the instrument. Silicon is possibly interacting with oxygen, but the amount of oxygen in the alloys is so small that this is difficult to detect. In prior work, the oxygen content of a similarly prepared $Cu_{47}Ti_{34}Zr_{11}Ni_8$ alloy was measured as <750 ppm atomic [73].

The APT data collected from the as-prepared (three samples) and the isothermally annealed (one sample) $Cu_{47}Ti_{33}Zr_{11}Ni_8Si_1$ samples were analyzed with the P_a and the LBM models (previously discussed in chapter 3.2). These data are shown in Table V for the P_a model and Table VI for the LBM model. Similar to the $Cu_{47}Ti_{34}Zr_{11}Ni_8$ samples (chapter 3.2), the $Cu_{47}Ti_{33}Zr_{11}Ni_8Si_1$ alloy exhibits decomposition primarily in copper and titanium in both the as-prepared and isothermally annealed states; this is evident by comparing the Δc values for each alloy. The as-prepared samples generally exhibit less decomposition than the isothermally annealed sample. Further analysis of the data with contingency tables showed that the copper and titanium are antisegregated; i.e., the copper-enriched regions are low in titanium and vice versa.

From the TEM work, after heat treatments at temperatures near the glass transition temperature, both alloys exhibit a face centered cubic phase in an amorphous matrix. The silicon in $Cu_{47}Ti_{33}Zr_{11}Ni_8Si_1$ delays the nucleation of this face centered cubic phase in $Cu_{47}Ti_{34}Zr_{11}Ni_8$ in the supercooled liquid. However, the silicon does not allow for a new primary nucleating phase to form.

as-prepared $Cu_{47}Ti_{33}Zr_{11}Ni_8Si_1$

	P_a	Standard error	χ^2	Degrees of freedom	$\Delta c = 2P_a$
Cu	0.080	0.009	15.3	23	0.160
Ti	0.093	0.012	21.6	25	0.186
Zr	0.013	0.009	11.2	13	0.026
Ni	0.044	0.003	**28.9**	15	0.088

as-prepared $Cu_{47}Ti_{33}Zr_{11}Ni_8Si_1$

	P_a	Standard error	χ^2	Degrees of freedom	$\Delta c = 2P_a$
Cu	0.061	0.006	29.6	26	0.122
Ti	0.055	0.006	20.6	26	0.110
Zr	0.008	0.009	16.9	14	0.016
Ni	0.017	0.002	4.1	11	0.034

as-prepared $Cu_{47}Ti_{33}Zr_{11}Ni_8Si_1$

	P_a	Standard error	χ^2	Degrees of freedom	$\Delta c = 2P_a$
Cu	0.075	0.004	**74.0**	31	0.150
Ti	0.079	0.004	**49.2**	34	0.158
Zr	0.028	0.002	21.6	19	0.056
Ni	0.014	0.002	9.8	14	0.028

isothermally annealed (708 K for 24 h) $Cu_{47}Ti_{33}Zr_{11}Ni_8Si_1$

	P_a	Standard error	χ^2	Degrees of freedom	$\Delta c = 2P_a$
Cu	0.106	0.007	**105.9**	34	0.212
Ti	0.100	0.007	**73.6**	34	0.200
Zr	0.028	0.003	12.9	18	0.056
Ni	0.029	0.001	**55.0**	14	0.058

The parameters P_a and Δc are given in atomic fraction. Bold entries in the χ^2 column indicate the fit is rejected at the 95% level.

Table V The results of the statistical analysis with the P_a model for $Cu_{47}Ti_{33}Zr_{11}Ni_8Si_1$

as-prepared $Cu_{47}Ti_{33}Zr_{11}Ni_8Si_1$

	b_1	b_2	σ	χ^2	Degrees of freedom	$\Delta c = b_1 + b_2$
Cu	0.030	0.080	0.030	10.656	23	0.110
Ti	0.130	0.020	0.050	15.314	24	0.150
Zr	0.010	0.010	0.010	11.645	13	0.020
Ni	0.050	0.020	0.010	19.239	15	0.070

as-prepared $Cu_{47}Ti_{33}Zr_{11}Ni_8Si_1$

	b_1	b_2	σ	χ^2	Degrees of freedom	$\Delta c = b_1 + b_2$
Cu	0.030	0.060	0.010	15.789	25	0.090
Ti	0.050	0.030	0.010	20.526	25	0.080
Zr	0.010	0.010	0.010	22.037	16	0.020
Ni	0.010	0.010	0.010	7.336	12	0.020

as-prepared $Cu_{47}Ti_{33}Zr_{11}Ni_8Si_1$

	b_1	b_2	σ	χ^2	Degrees of freedom	$\Delta c = b_1 + b_2$
Cu	0.030	0.050	0.040	42.905	33	0.080
Ti	0.050	0.040	0.040	37.255	35	0.090
Zr	0.030	0.010	0.010	19.002	19	0.040
Ni	0.010	0.010	0.010	15.237	14	0.020

isothermally annealed (708 K for 24 h) $Cu_{47}Ti_{33}Zr_{11}Ni_8Si_1$

	b_1	b_2	σ	χ^2	Degrees of freedom	$\Delta c = b_1 + b_2$
Cu	0.040	0.090	0.050	27.984	35	0.130
Ti	0.110	0.030	0.050	20.860	36	0.140
Zr	0.040	0.010	0.010	10.874	19	0.050
Ni	0.010	0.040	0.010	13.127	13	0.050

The parameters b_1, b_2, σ, and Δc are given in atomic fraction.

Table VI The results of the statistical analysis with the LBM model for

$Cu_{47}Ti_{33}Zr_{11}Ni_8Si_1$

The covalent bonding nature of silicon could be delaying the onset of nucleation of an intermetallic crystalline phase as the metal is cooled from the liquid. Choi-Yim et al. [72] observed that the thermodynamics and kinetics of $Cu_{47}Ti_{34}Zr_{11}Ni_8$ and $Cu_{47}Ti_{33}Zr_{11}Ni_8Si_1$ do not significantly differ near the glass transition temperature. However, at a temperature closer to the liquidus temperature, perhaps the silicon addition is frustrating the formation of a crystalline phase, improving the glass-forming ability of the alloy. Another possibility, as was previously hypothesized, is that silicon is destabilizing oxide nucleation sites in $Cu_{47}Ti_{34}Zr_{11}Ni_8$, leading to improvements in thermal stability of the supercooled liquid against crystallization and glass-forming ability.

4.2. Magnesium and Germanium Additions to $Cu_{47}Ti_{34}Zr_{11}Ni_8$

Magnesium was chosen as an alloying addition to $Cu_{47}Ti_{34}Zr_{11}Ni_8$ because of magnesium's chemical affinity for oxygen, as shown in an Ellingham diagram [74]. Germanium was chosen as an alloying addition because it has the same covalent bonding nature as silicon, which may influence the glass-forming ability of the alloy.

Alloys of nominal compositions $Cu_{47}Ti_{34}Zr_{11}Ni_8$, $Cu_{47}Ti_{34-x}Zr_{11}Ni_8Mg_x$ (x = 0.25, 0.5, 1, 1.5, 2), and $Cu_{47}Ti_{34-x}Zr_{11}Ni_8Ge_x$ (x = 1, 2, 4) were prepared in an arc melter with a titanium gettered, ultrahigh purity argon atmosphere, with elements of purities from 99.9% to 99.9999%. The magnesium alloys were prepared by melting all of the alloy components together. Due to the high vapor pressure of magnesium, magnesium was placed under the other elemental metals so that it did not melt first and boil off. To make the germanium alloys, the germanium was first melted with copper to avoid forming any

high melting point germanides; the other components of the alloy were alloyed with each other as well. Then, the two ingots were alloyed to obtain the desired composition. All ingots were flipped and remelted at least twice to promote homogeneity.

In an attempt to obtain amorphous alloys, the alloys were remelted in fused quartz tubes in a high frequency induction furnace and then injection cast with ultrahigh purity argon into a copper mold of dimensions 1 × 4 × ~25 mm (thickness by width by length). Differential scanning calorimetry (*Perkin Elmer DSC-7*), differential thermal analysis (*Perkin Elmer DTA-7*), and X-ray diffraction (*Inel PSD* with a cobalt source) were used to characterize the alloys. For the DTA work, graphite crucibles machined from *POCO DFP-1* graphite were used.

DSC scans (heating rate of 0.333 K/s) of $Cu_{47}Ti_{34-x}Zr_{11}Ni_8Mg_x$ (x = 0.25, 0.5, 1, 1.5, 2) and $Cu_{47}Ti_{34-x}Zr_{11}Ni_8Ge_x$ (x = 1, 2, 4) cast into 1 mm thick strips are shown in Figs. 26 and 27, respectively. Arrows indicate the onset of the glass transition and crystallization.

The magnesium alloys with 0.5% and 1.0% magnesium show a slight increase in the temperature interval between the onset of the glass transition and crystallization, ΔT. However, it is likely that all of the magnesium was boiled out of the magnesium alloys. An electron probe microanalysis (*Jeol JXA-733 electron microprobe*) revealed no magnesium in any of the magnesium alloys, and the mass loss during alloying from each ingot corresponded to the mass of magnesium in the alloy.

In experiments performed by Bossuyt [75] on $Cu_{47}Ti_{34}Zr_{11}Ni_8$, 1 at. % of one element was removed and 1% of one constituent element was added (e.g., 1% at. Ti removed and 1% Zr added), yielding a total of twelve different compositions. In the

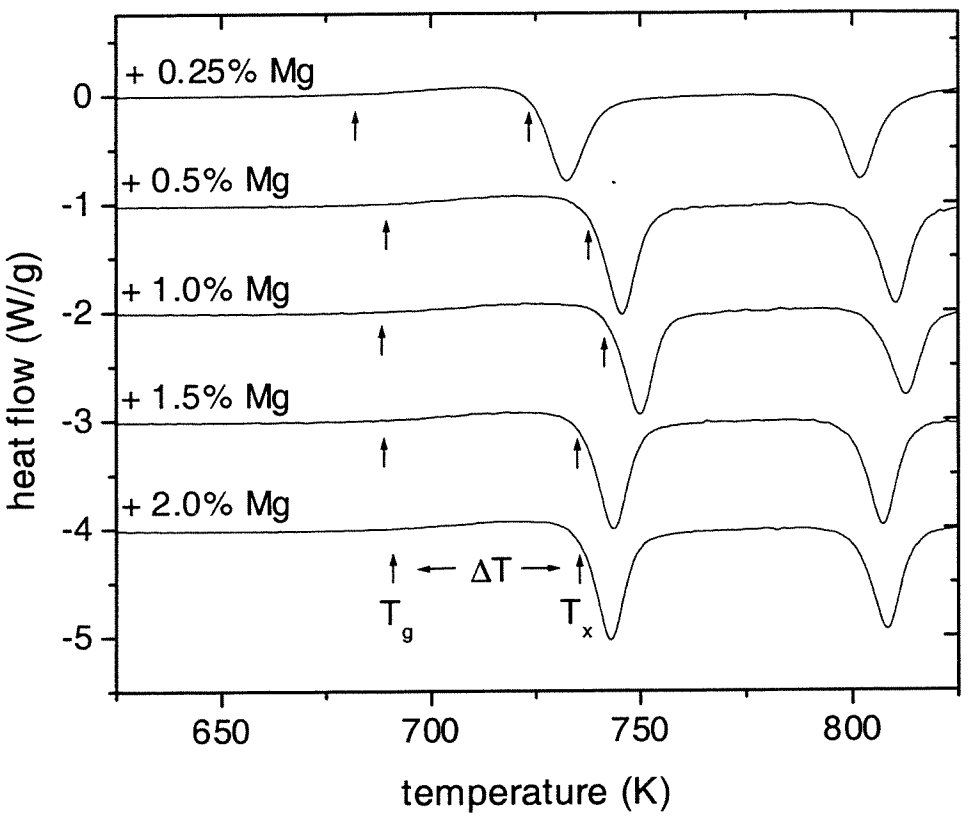

Fig. 26 DSC scans of $Cu_{47}Ti_{34-x}Zr_{11}Ni_8Mg_x$ (x = 0.25, 0.5, 1, 1.5, 2) alloys

DSC scans (heating rate of 0.333 K/s) of material cast into a 1 mm strip. Arrows indicate the onset of the glass transition, T_g, and crystallization, T_x.

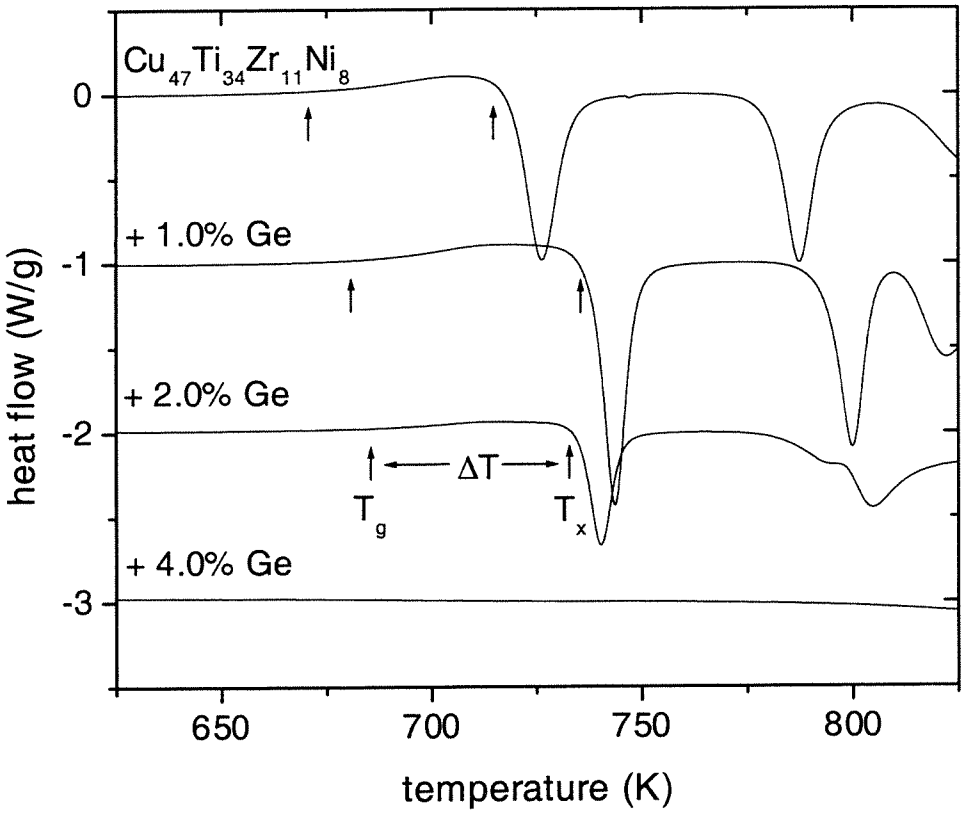

Fig. 27 DSC scans of $Cu_{47}Ti_{34}Zr_{11}Ni_8$ and $Cu_{47}Ti_{34-x}Zr_{11}Ni_8Ge_x$ (x = 1, 2, 4) alloys

DSC scans (heating rate of 0.333 K/s) of material cast into a 1 mm strip. Arrows indicate the onset of the glass transition, T_g, and crystallization, T_x.

alloys in which titanium was removed, increases in the critical casting thickness, corresponding to an improvement in the glass-forming ability of the alloy, were observed. Thus, the exact role that magnesium plays in this increase in ΔT for the 0.5% and 1.0% magnesium alloys is not clear.

For the germanium alloys, the 1.0% germanium alloy has the largest ΔT. The 2.0% germanium alloy could be fabricated into a partially amorphous solid, as evidenced by the exothermic crystallization peaks. X-ray diffraction indicated crystals in this sample. The 4.0% germanium alloy could not be made amorphous by casting into a 1 mm strip.

DTA scans for $Cu_{47}Ti_{34-x}Zr_{11}Ni_8Mg_x$ (x = 0.25, 0.5, 1, 1.5, 2) and $Cu_{47}Ti_{34-x}Zr_{11}Ni_8Ge_x$ (x = 1, 2, 4) are shown in Figs. 28 and 29, respectively. Arrows indicate the solidus and liquidus temperatures. The DTA scans for the magnesium containing alloys were performed at a heating rate of 0.167 K/s, while the DTA scans for the germanium containing alloys were performed at a heating rate of 0.333 K/s. For the magnesium containing alloys, there were no significant changes in the solidus and liquidus temperatures with increasing magnesium content. Increasing germanium additions to $Cu_{47}Ti_{34}Zr_{11}Ni_8$ slightly increased the solidus and the liquidus temperatures of the alloy. The large exotherm after melting of the germanium alloys is attributed to the alloy reacting with the graphite crucible.

Magnesium could intentionally be boiled out of the magnesium containing alloys. One ingot of $Cu_{47}Ti_{34}Zr_{11}Ni_8$ was made and then placed on top of block of magnesium in the arc melter. By repeatedly melting this mass, all of the magnesium was eventually

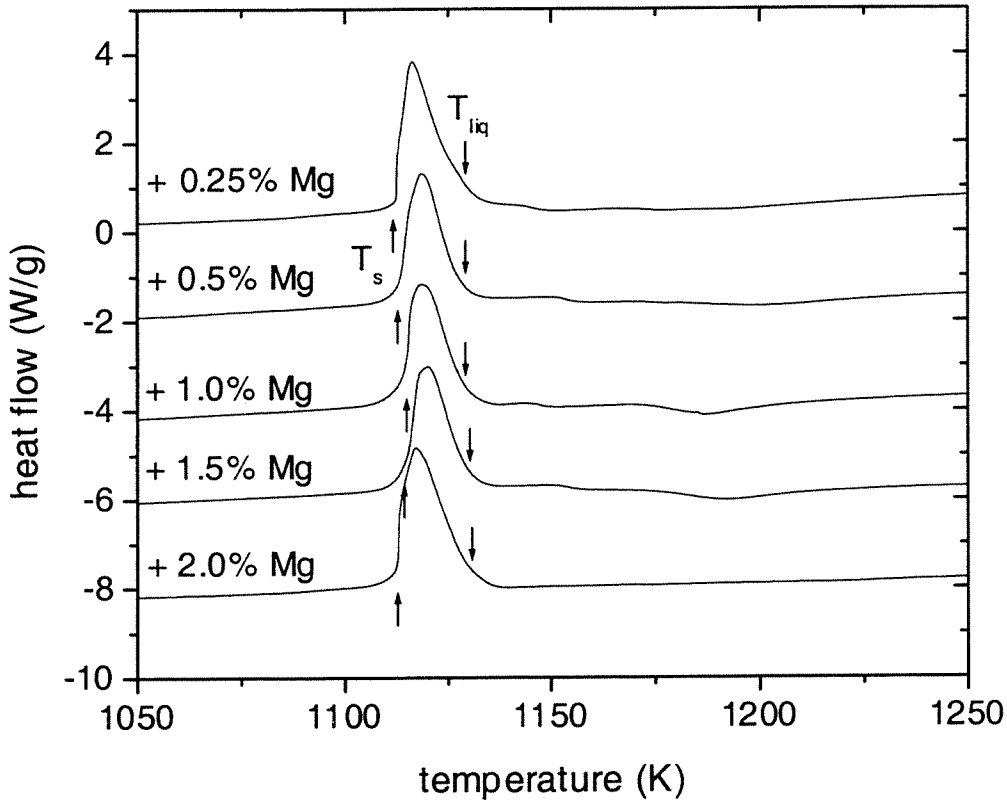

Fig. 28 DTA scans of $Cu_{47}Ti_{34-x}Zr_{11}Ni_8Mg_x$ (x = 0.25, 0.5, 1, 1.5, 2) alloys

DTA scans were performed at a heating rate of 0.167 K/s. Arrows indicate the solidus temperature, T_s, and the liquidus temperature, T_{liq}.

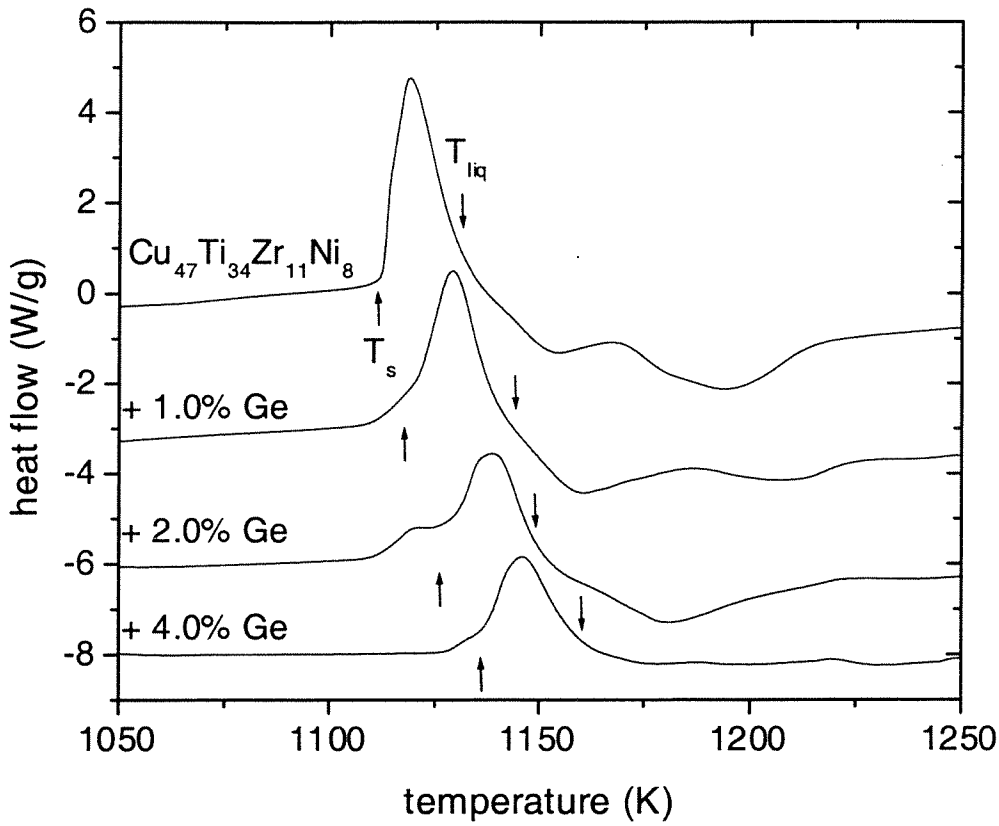

Fig. 29 DTA scans of $Cu_{47}Ti_{34}Zr_{11}Ni_8$ and $Cu_{47}Ti_{34-x}Zr_{11}Ni_8Ge_x$ (x = 1, 2, 4) alloys

DTA scans were performed at a heating rate of 0.333 K/s. Arrows indicate the solidus temperature, T_s, and the liquidus temperature, T_{liq}.

removed. To determine whether there was any improvement in the glass-forming ability, the ingot was cast into a wedge shaped mold to determine the maximum casting thickness. The maximum casting thickness was not greater than that of a $Cu_{47}Ti_{34}Zr_{11}Ni_8$ ingot that had not gone through this treatment; there was no improvement in the glass-forming ability.

The 1.0% germanium alloy was the most promising composition for improvements in the glass-forming ability of $Cu_{47}Ti_{34}Zr_{11}Ni_8$ because of its stability in the supercooled liquid. To test the glass-forming ability of the $Cu_{47}Ti_{33}Zr_{11}Ni_8Ge_1$ alloy, the alloy was cast in a 5 mm thick strip. In the previous work performed with silicon, the $Cu_{47}Ti_{33}Zr_{11}Ni_8Si_1$ alloy could be cast in a 5 mm amorphous strip whereas $Cu_{47}Ti_{34}Zr_{11}Ni_8$ could not be, indicating an improvement in the glass-forming ability due to the silicon addition. $Cu_{47}Ti_{33}Zr_{11}Ni_8Ge_1$ could not be cast into a 5mm thick amorphous strip. Although ΔT for this alloy increased, there was no measurable improvement in the glass-forming ability.

Glass-forming ability is taken as the ability of an alloy to bypass crystallization when cooled from the melt. A high glass-forming ability is manifested by a large casting thickness. To achieve a large casting thickness, the liquid must be cooled rapidly enough to bypass the nose of the TTT diagram (Fig. 1) associated with the competing crystalline phases. ΔT, the temperature interval between the onset of glass transition and crystallization, is a measure of the thermal stability of a glass with respect to crystallization. This is a commonly used parameter to measure the glass-forming ability of an alloy. However, a larger ΔT for an alloy only indicates that the supercooled liquid is more stable against crystallization than an alloy with a smaller ΔT. The critical

temperature regime for forming a glass from the melt is the temperature interval between the melting temperature and the glass transition temperature.

As previously discussed (chapter 2.2), one indicator of the glass-forming ability of an alloy is the reduced glass transition temperature, T_{rg}. The reduced glass transition temperature is given by

$$T_{rg} = \frac{T_g}{T_m}, \tag{31}$$

where T_g is the glass transition temperature and T_m is the melting temperature. Larger reduced glass transition temperatures often indicate better glass-forming ability; the temperature interval between the glass transition temperature and melting temperature is smaller, decreasing the likelihood of crystallization. The reduced glass transition temperature thus gives a measure of the likelihood of quenching a metallic liquid to the glassy state at a specific cooling rate. T_{rg} for $Cu_{47}Ti_{34}Zr_{11}Ni_8$ is 0.60. All of the alloys in this study have the same reduced glass transition temperature within the experimental error of the instruments used.

The results in Fig. 26 for the $Cu_{47}Ti_{34-x}Zr_{11}Ni_8Mg_x$ alloys indicate that the thermal stability of the supercooled liquid against crystallization may be improved by alloying with magnesium. The electron probe microanalysis revealed no magnesium in these alloys, so one possible reason for this improvement in the stability of the supercooled liquid is the small change in composition of the alloy, i.e., the lower amount of titanium in the alloy. Another possiblity is that magnesium has a fluxing effect in the molten

liquid; i.e., the magnesium bonds with oxygen in the melt and then evaporates, removing oxide catalytic nucleation sites.

The results in Fig. 27 for the $Cu_{47}Ti_{34-x}Zr_{11}Ni_8Ge_x$ alloys show that $Cu_{47}Ti_{33}Zr_{11}Ni_8Ge_1$ does have a larger ΔT than $Cu_{47}Ti_{34}Zr_{11}Ni_8$, but an improvement in the glass-forming ability similar to $Cu_{47}Ti_{33}Zr_{11}Ni_8Si_1$ was not observed. The trends established in Fig. 27 warrant further investigation. With the experiments performed thus far, the role of silicon in the alloy may be different than that of magnesium or germanium.

5. SUMMARY

The $Cu_{47}Ti_{34}Zr_{11}Ni_8$ glass-forming alloy was extensively studied. By measuring the specific heat capacity of the liquid and the crystalline states, the differences in the thermodynamic functions between the liquid and the crystalline states were calculated. In general, the lower Gibbs free energy difference between the liquid and the crystalline states, the better the glass-forming ability of an alloy. Also, in general, the lower the entropy of fusion of the crystalline state, the better the glass-forming ability of an alloy. The viscosity of $Cu_{47}Ti_{34}Zr_{11}Ni_8$ was measured, which also gives an indicator of the glass-forming ability of a system.

Different experimental techniques were used to investigate the crystallization of amorphous $Cu_{47}Ti_{34}Zr_{11}Ni_8$. Similar to other metallic glass-forming alloys, $Cu_{47}Ti_{34}Zr_{11}Ni_8$ phase separates prior to crystallization. $Cu_{47}Ti_{34}Zr_{11}Ni_8$ decomposes to copper-enriched and titanium-enriched regions (the copper-enriched regions are low in titanium content and vice versa). The primary nucleating phase has a face centered cubic structure.

Small additions of silicon to $Cu_{47}Ti_{34}Zr_{11}Ni_8$ have previously been shown to improve thermal stability of the alloy against crystallization and the glass-forming ability of the alloy. Both $Cu_{47}Ti_{34}Zr_{11}Ni_8$ and $Cu_{47}Ti_{33}Zr_{11}Ni_8Si_1$ decompose to copper-enriched and titanium-enriched regions prior to crystallization. Both alloys exhibit a face centered cubic primary nucleating phase. No change in the local composition around a silicon atom in $Cu_{47}Ti_{33}Zr_{11}Ni_8Si_1$ was detected. Silicon is possibly destabilizing oxide

nucleation sites in $Cu_{47}Ti_{34}Zr_{11}Ni_8$, leading to the observed improvements in the thermal stability of the alloy.

Small additions of magnesium and germanium were made to $Cu_{47}Ti_{34}Zr_{11}Ni_8$ to determine if these elements had a similar effect as that of silicon. No improvements in the glass-forming ability were observed for either addition. However, the thermal stability of the supercooled liquid against crystallization was improved with both the magnesium and germanium additions. The results on $Cu_{47}Ti_{33}Zr_{11}Ni_8Ge_1$ warrant further investigation.

6. APPENDIX: OTHER PROPERTIES OF $Cu_{47}Ti_{34}Zr_{11}Ni_8$

density, ρ	6.85 g/cm^3
Vicker's hardness, H_v [14]	628 ± 20 kg/mm^2

The surface tension [76] and the thermal expansion coefficient [77] of $Cu_{47}Ti_{34}Zr_{11}Ni_8$ were also measured with the TEMPUS experimental facility.

7. REFERENCES

[1] D.R. Uhlmann, J. Non-Cryst. Solids, **7**, 337 (1972).

[2] W. Klement, R.H. Willens, and P. Duwez, Nature **187**, 869 (1960).

[3] W.H. Zachariasen, J. Am. Chem. Soc. **54**, 3841 (1932).

[4] T. Zhang, A. Inoue, and T. Masumoto, Mater. Trans., JIM **32**, 1005 (1991).

[5] A. Peker and W.L. Johnson, Appl. Phys. Lett. **63**, 2342 (1993).

[6] A. Inoue, N. Nishiyama, and H. Kimura, Mater. Trans., JIM **38**, 179 (1997).

[7] J. Schroers, R. Busch, A. Masuhr, and W.L. Johnson, Appl. Phys. Lett. **74**, 2806 (1999).

[8] A. Inoue, Mater. Trans. JIM **36**, 866 (1995).

[9] A.L. Greer, Science **267**, 1947 (1995).

[10] M.H. Cohen and D. Turnbull, Nature **189**, 131 (1961).

[11] T.B. Massalski, ed., *Binary Alloy Phase Diagrams*, 2nd ed. (ASM International, Metals Park, 1990).

[12] C.G. Woychik and T.B. Massalski, Z. Metal. **79**, 149 (1988).

[13] P. Villars, A. Prince, and H. Okamoto, *Handbook of Ternary Alloy Phase Diagrams* (ASM International, Metals Park, 1997).

[14] X.H. Lin and W.L. Johnson, J. Appl. Phys. **78**, 6514 (1995).

[15] X.H. Lin, Ph.D. thesis, California Institute of Technology, 1997.

[16] C.C. Hays, S. Bossuyt, S.C. Glade (unpublished research, 2000).

[17] A. Einstein, *Investigations on the Theory of the Brownian Movement* (Dover, New York, 1956).

[18] R. Busch, W. Liu, and W.L. Johnson, J. Appl. Phys. **83**, 4134 (1998).

[19] H.J. Fecht and W.L. Johnson, Rev. Sci. Instrum. **62**, 1299 (1991).

[20] R.K. Wunderlich and H.J. Fecht, Int. J. Thermophys. **17**, 1203 (1996).

[21] J. Szekely, E. Schwartz, and R. Hyers, JOM **47**, 50 (1995).

[22] J. Pillar, A. Seidel, M. Stauber, and W. Dreier, in *Solidification 99*, edited by S.P. Marsh, N.B. Singh, P.W. Voorhees, and W.H. Hofmeister (TMS Publications, 1999), p. 3.

[23] S.C. Glade, D.S. Lee, R. Wunderlich, and W.L. Johnson, Mat. Res. Soc. Symp. Proc. **551** (Warrendale, PA, 1999), p. 219.

[24] R.K. Wunderlich, R.A. Sagel, C. Ettel, H.-J. Fecht, D.S. Lee, S. Glade, and W.L. Johnson, in *Solidification 99*, edited by S.P. Marsh, N.B. Singh, P.W. Voorhees, and W.H. Hofmeister (TMS Publications, 1999), p. 53.

[25] R. K. Wunderlich, H.-J. Fecht, S.C. Glade, and W.L. Johnson, in *Proceedings, EUROMAT: European Congress on Advanced Materials and Processing* (VCH-Wiley).

[26] O. Kubaschewski, C.B. Alcock, P.J. Spencer, *Materials Thermochemistry*, 6th ed. (Permagon, New York, 1993).

[27] W. Kauzmann, Chem. Rev. **43**, 219 (1948).

[28] S.C. Glade, R. Busch, D.S. Lee, W.L. Johnson, R.K. Wunderlich, and H.J. Fecht, J. Appl. Phys. **87**, 7242 (2000).

[29] D. Turnbull, J. Appl. Phys. **21**, 1022 (1950).

[30] D. Turnbull, Contemp. Phys. **10**, 473 (1969).

[31] R. Busch, Y.J. Kim, and W.L. Johnson, J. Appl. Phys. **77**, 4039 (1995).

[32] H.A. Barnes, J.F. Hutton, and K. Walters, *An Introduction to Rheology* (Elsevier, Amsterdam, 1989).

[33] F.T. Trouon, Proc. R. Society London **77**, 426 (1906).

[34] M. Reiner, in *Rheology*, Edited by F.R. Eirich (Academic Press Inc., New York, 1956), Vol. 1, p. 9.

[35] H.E. Hagy, J. Am. Ceram. Soc. **46**, 93 (1963).

[36] R. Busch and W.L. Johnson, Appl. Phys. Lett. **72,** 2695 (1998).

[37] I. Egry, J. Non-Cryst. Solids **250**, 63 (1999).

[38] H. Vogel, Phys. Z. **22**, 645 (1921).

[39] G.S. Fulcher, J. Amer. Ceram. Soc. **8**, 339 (1925).

[40] G. Tamman and G. Hesse, Z. Anorg. Allg. Chem. **156**, 245 (1926).

[41] L. Battezzati and A.L. Greer, Acta. Metall. Mater. **37**, 1791 (1989).

[42] C.A. Angell, Science **267**, 1924 (1995).

[43] S. Glasstone, K.J. Laidler, and H. Eyring, *The Theory of Rate Processes* (McGraw-Hill, New York, 1941).

[44] T.A. Waniuk, R. Busch, A. Masuhr, and W.L. Johnson, Acta Mater. **46**, 5229 (1998).

[45] R. Busch, E. Bakke, and W.L. Johnson, Acta Mater. **46**, 4725 (1998).

[46] T.A. Waniuk (private communication, 2000).

[47] W.L. Johnson, MRS Bulletin **24**, 42 (1999).

[48] S. Schneider, P. Thiyagarajan, and W.L. Johnson, Appl. Phys. Lett. **68**, 493 (1996).

[49] M.P. Macht, N. Wanderka, A. Wiedenmann, H. Wollenberger, Q. Wei, H.J. Fecht, and S.G. Close, Mater. Sci. Forum **225-227**, 65 (1996).

[50] W. Liu and W.L. Johnson, J. Mater. Res. **11**, 2388 (1996).

[51] J.F. Löffler, S. Bossuyt, S.C. Glade, W.L. Johnson, W. Wagner, and P. Thiyagarajan, Appl. Phys. Lett. **77**, 525 (2000).

[52] M. Calin and U. Köster, Mater. Sci. Forum **269-272**, 749 (1998).

[53] S. Schneider, P. Thiyagarajan, U. Geyer, and W.L. Johnson, Physica B **241-243**, 918 (1998).

[54] K.F. Kelton, Philos. Mag. Lett. **77**, 337 (1998).

[55] J.F. Löffler and W.L. Johnson, Appl. Phys. Lett. **76**, 3394 (2000).

[56] P. Thiyagarajan, J.E. Epperson, R.K. Crawford, J.M. Carpenter, T.E. Klippert, and D. G. Wozniak, J. Appl. Cryst. **30**, 280 (1997).

[57] S. Schneider, U. Geyer, P. Thiyagarajan, R. Busch, R. Schulz, K. Samwer, and W.L. Johnson, Mater. Sci. Fourm **225-227**, 59 (1996).

[58] J.M. Sassen, M.G. Hetherington, T.J. Godfrey, G.D.W. Smith, P.H. Pumphrey, and K.N. Akhurst in *Properties of Stainless Steels in Elevated Temperature Service*, edited by M. Prager (American Society of Mechanical Engineers, New York, 1987), p. 65.

[59] J.S. Langer, M. Bar-on, and H.D. Miller, Phys. Rev. A **11**, 1417 (1975).

[60] M.K. Miller, A. Cerezo, M.G. Hetherington, and G.D.W. Smith, *Atom Probe Field Ion Microscopy* (Oxford, Oxford, 1996).

[61] M.K. Miller, K.O. Bowman, A. Cerezo, and J.M. Hyde, Appl. Surf. Sci. **67**, 429 (1993).

[62] Y.J. Kim, R. Busch, W.L. Johnson, A.J. Rullison, and W.K. Rhim, Appl. Phys. Lett. **65**, 2136 (1994).

[63] TAPP, ver. 2.2, E S Micoware, Inc., Hamilton, OH (1994).

[64] M.K. Miller, K.F. Russell, P.M. Martin, R. Busch, and W.L. Johnson, J. Phys. IV **6**, (C5) 217 (1996).

[65] E.L. Huston, J.W. Cahn, and J.E. Hillard, Acta. Met. **14**, 1053 (1966).

[66] S. Bossuyt, J.F. Löffler, S.C. Glade, W.L. Johnson, S. Seifert, and P. Thiyagarajan (unpublished research).

[67] E. Budke, P. Felitz, M.P. Macht, V. Naundorf, and G. Frohberg, Defect and Diff. Forum **143-147**, 825 (1997).

[68] A. Inoue, T. Aoki, and H. Kimura, Mater. Trans. JIM **38**, 175 (1997).

[69] A. Inoue, T. Nefishi, H. Kimura, and T. Aoki, Mater. Trans. JIM **38**, 185 (1997).

[70] X.H. Lin, W.L. Johnson, and W.K. Rhim, Mater. Trans. JIM **38**, 473 (1997).

[71] C.A. Volkert, Ph.D. thesis, Harvard University, 1988.

[72] H. Choi-Yim, R. Busch, and W.L. Johnson, J. Appl. Phys. **83**, 7993 (1998).

[73] S.C. Glade (unpublished research, 1997).

[74] D. Gaskell, *Introduction to Metallurgical Thermodynamics* (Hemisphere Publishing Co., New York, 1981).

[75] S. Bossuyt (unpublished research, 2000).

[76] M. Rösner-Kuhn, G. Kuppermann, and M.G. Frohberg, Microgravity Science Laboratory (MSL-1) Final Report, NASA/CP-1998-208868, 332 (1998).

[77] B. Damaschke and K. Samwer, Appl. Phys. Lett. **75**, 2220 (1999).